HYBRID NANOSCALE DEVICES FOR MAGNETOCALORIC REFRIGERATION

by

Kellen Malone

A thesis submitted to the Faculty and the Board of Trustees of the Colorado School of Mines in partial fulfillment of the requirements for the degree of Master of Science (Applied Physics).

Golden, Colorado

Date _____

Signed: _____
Kellen Malone

Signed: _____
Dr. Meenakshi Singh
Thesis Advisor

Golden, Colorado

Date _____

Signed: _____
Dr. Uwe Greife
Professor and Head
Department of Physics

ABSTRACT

Refrigeration is one of the main technologies contributing to climate change because of its use of greenhouse gases. Magnetic cooling provides an alternative refrigeration method that is more energy efficient than standard refrigeration technologies, and magnetocaloric materials have proven to be some of the best candidate materials for magnetic cooling. In an effort to make magnetocaloric materials a viable option for refrigeration, alternative methods of driving the magnetocaloric effect, specifically with voltage and stress, are analyzed through simulations and experiments on two hybrid material devices. The results indicate that the concept of voltage induced stress to drive the magnetocaloric effect is plausible. Further materials research is required to find a material combination that can compete with existing refrigeration technology.

TABLE OF CONTENTS

LIST OF FIGURES

LIST OF TABLES

LIST OF ABBREVIATIONS

Chlorofluorocarbon . . . . . CFC

Hydrochlorofluorocarbon . . . . . HCFC

Vanadium Dioxide . . . . . VO_2

Nickel . . . . . Ni

Lead Zirconate Titanate . . . . . PZT

Magnetocaloric Effect . . . . . MCE

Monte Carlo . . . . . MC

Adiabatic Demganetization Refrigeration . . . . . ADR

ACKNOWLEDGMENTS

I would like to thank the Colorado Energy Research Collaboratory for funding this project. This project would never have succeeded without my advisors Meenakshi Singh, Nitin Kumar, and Geoff Brennecka, collaborators Jose De La Venta, Josh Lauzier, and Logan Sutton, research group especially George Smith, Kirsten Blagg, and Portia Allen, and the constant support of my family and friends.

It takes a village to raise a child.

CHAPTER 1

INTRODUCTION

1.1 Overview and Motivation

In a 2018 study, the non-profit "Drawdown" placed refrigeration management as the number one solution to reducing the impact of climate change[1]. This is due to the large carbon footprint of refrigerators, coupled with the ozone-depleting capabilities of popular refrigerants (Chlorofluorocarbons (CFCs), Hydrochlorofluorocarbons (HCFCs)...). Interest in magnetic refrigeration for cooling began when it was shown that solid-state magnetic cooling had the potential to be more energy efficient (and therefore have a smaller carbon footprint during operation) than house-hold vapor compression refrigeration[2, 3]. Solid-state magnetic refrigeration cycles also do not require environmentally harmful refrigerants, which makes them doubly advantageous over vapor compression. Leading the field of magnetic refrigeration materials are magnetocaloric materials. These materials possess a pronounced magnetocaloric effect, which will be discussed in further detail in the next chapter. The discovery of the giant magnetocaloric effect (MCE) in $Gd_5Si_2Ge_2$ sparked a renewed interest in room temperature refrigeration using magnetocaloric materials as this was the first material that experimentally demonstrated a large temperature change near room temperature[4]. Even though there have been numerous breakthroughs in magnetocaloric materials research since then, there are still challenges to overcome in order to further the development of commercially viable magnetocaloric refrigerators. One of these challenges is having to rely on large external magnetic fields to drive the MCE. Traditional MCE materials require at-least 1 Tesla magnetic field changes to produce an appreciable temperature change. This project seeks to explore whether it is possible to overcome this challenge by using multiferroic hybrid nanostructures. Magnetic properties of these nanostructures can be controlled with voltage or stress, leading the way to new avenues in MCE research by eliminating the need for

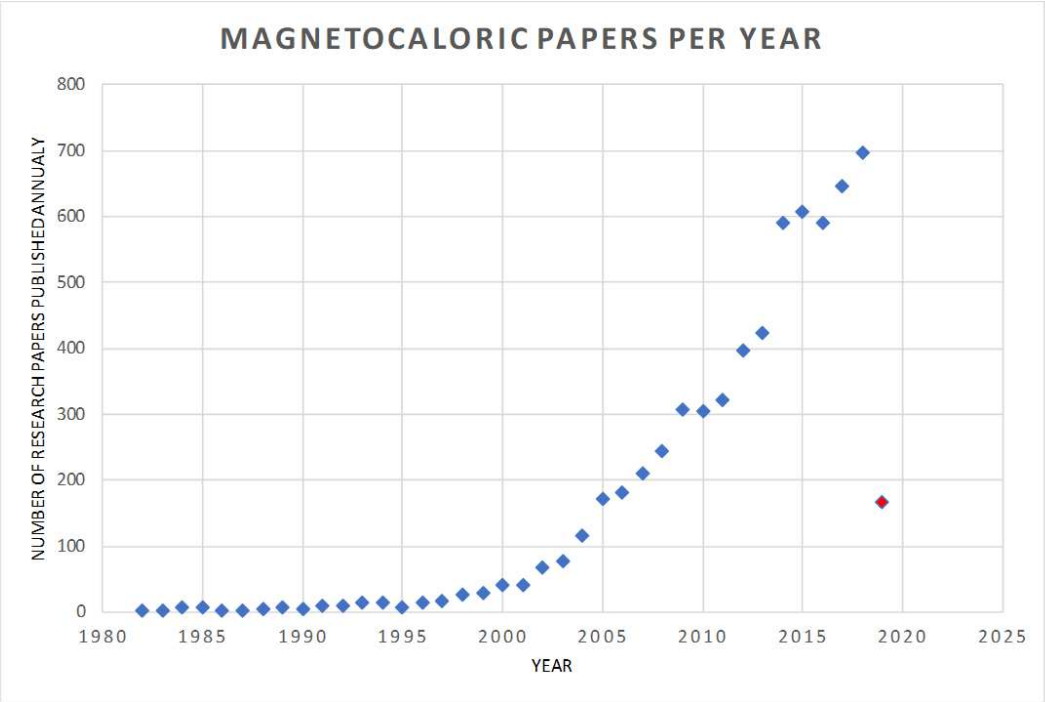

Figure 1.1: The number of papers published per year within the magnetocaloric field. The red dot is the number of papers published in 2019 as of March. The giant MCE was discovered in $Gd_5Si_2Ge_2$ in 1995.

large magnetic fields and opening up the possibility of using other mechanisms to drive the MCE. Evidence of using structural phase transitions of substrates to affect magnetic properties of ferromagnets has been realized by collaborators at CSU, Jose De La Venta, Josh Lauzier, and Logan Sutton. For example, Nickel deposited on a VO_2 substrate demonstrates a measurable change in coercivity before and after the VO_2 substrate undergoes a structural phase transition and applies a stress to the Nickel, seen in Figure 1.2[5]. This system will be explained in more detail in the following chapters.

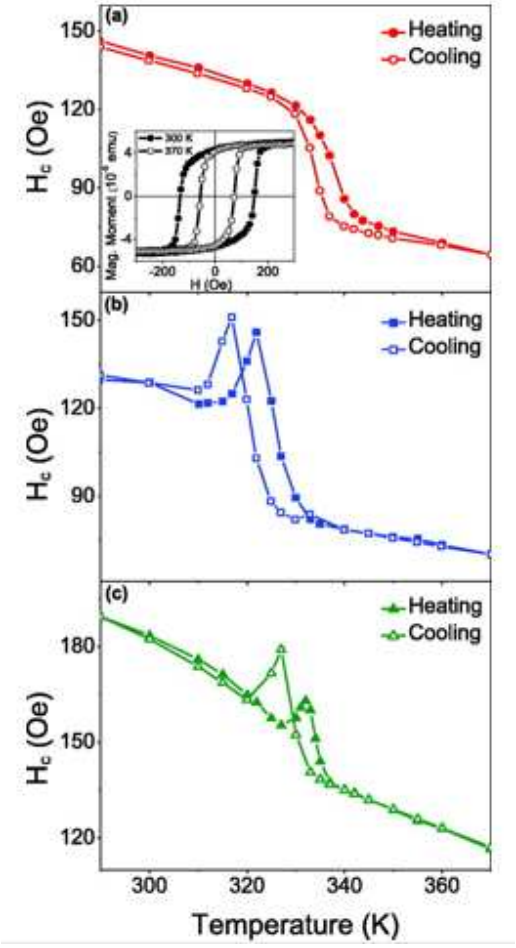

Figure 1.2: Plots of coercivity field H_c in Nickel vs Temperature of VO_2/Ni on different substrates. The three substrates used are (red) Al2O3 (001); (blue) TiO2 (101); and (green) Al2O3 (012)

1.2 Objectives of Research

The goal of this Masters Thesis project is to analyze an alternative method of employing the MCE for magnetic cooling. Instead of driving the MCE with magnetic fields, it is possible to drive it with voltage. Since it is more energy efficient to generate electric rather than magnetic fields, voltage-driven magnetic cooling has the potential to be more energy efficient than standard magnetic cooling. To analyze this alternative method, two candidate systems, VO_2/Ni and PZT/Ni are analyzed. We are interested in the VO_2/Ni material system because VO_2 has a structural phase transition near room temperature that can be driven with voltage. We are also interested in the PZT/Ni system because PZT it is an insulating piezoelectric that undergoes a deformation with an applied voltage. Both systems apply stress on the Nickel from an applied voltage that can change the magnetic properties of the Nickel. Here, stress is the intermediary between voltage and the MCE.

The computational approach of this project entails (1) simulating the stress profile of VO_2 as it undergoes its phase transition, and (2) simulating the thermodynamic and magnetic properties of Nickel under applied stress, in order to predict relevant properties of the material systems and develop models for future material searches if the current hybrid systems do not meet our criteria. The experimental approach entails conducting measurements on (1) the VO_2 phase transition and on (2) the PZT/Ni temperature change.

1.3 Organization of Thesis

The organization of this thesis begins with the literature review and background section in Chapter 2. Chapter 3 discusses simulations of the two systems. Chapter 4 describes the experimental set-up and results of measurements on both systems. Chapter 5 covers conclusions and future outlook of the project.

CHAPTER 2

BACKGROUND

2.1 History Of Magnetic Refrigeration

The origins of the discovery of the magnetocaloric effect can be traced back to James Joule, who in 1843 found that electrical currents, even electromagnetically induced currents, will produce heat within a material[6, 7]. This led to the idea that repeated magnetizations and demagnetizations of a ferromagnetic material will overall increase the ferromagnet's temperature. This occurs because the induction currents that form from varying the magnetic field within the ferromagnet will dissipate heat within the material. This is not the magnetocaloric effect, but the first identification of a physical principle that relates magnetic and thermodynamic properties of a material.

A few decades later, William Thomson (Lord Kelvin) figured out another way magnetic fields could change a material's temperature. Thomson observed that ferromagnetic materials demonstrate an abrupt decrease in magnetization at high enough temperatures. He used this observation and thermodynamics to deduce how an external magnetic field would affect the temperature of a material through the temperature dependence of the material's magnetization[8]. Through further experimentation he came to the realization that bringing ferromagnetic materials closer (further) from magnets would increase (decrease) the material's temperature[9]. He further noted that this effect was most pronounced around the temperature that the ferromagnet has an abrupt decrease in magnetization.

Even though Thomson had discovered many of the characteristics of the magnetocaloric effect by the 1860's, a device that could utilize thermodynamic properties to change magnetic properties (or vice versa) did not appear until Edison and Tesla both patented a 'pyromagnetic generator' in the late 1880's[10, 11]. This generator was capable of taking heat and converting it into electric power.

After the turn of the 20th century, Weiss and Piccard were able to experimentally measure the temperature change in Nickel due to a changing magnetic field, and in doing so coined the phrase "magnetocaloric effect" for this phenomenon[12]. They derived a thermodynamic relation for the temperature change of the magnetocaloric effect and attributed it to Langevin's molecular field of ferromagnets[13].

With all of the theoretical pieces in place, Giaque and MacDougall experimentally demonstrated adiabatic demagnetization on paramagnetic salts[14]. This process lowered the temperature of the salts from 4K to 1K, and was the first experiment to realize magnetic refrigeration, but unfortunately the process could not be used near room temperature. Above low temperatures, the magnetocaloric temperature change, using the strongest magnetic fields that could be generated at the time, is so small that it would not be noticeable at room temperature unless the material's Curie temperature was about room temperature.

No known material had demonstrated a near-room temperature Curie temperature until Brown showed that Gadolinium had a Curie temperature around 290 K[15]. Other more common ferromagnetic materials like Iron, Nickel, and Cobalt for example, have Curie temperatures of 1043, 631, and 1400 K respectively. Pecharsky and Gschneider followed by measuring a 'giant' magnetocaloric effect in $Gd_5Si_2Ge_2$, sparking a revived interest in magnetocaloric materials and magnetic refrigeration[4].

2.2 Vapor Compression Refrigeration

Before diving into what the Magnetocaloric effect is, we will start with a brief description of standard vapor compression technology and vapor compression cycles. This will help to showcase the similarities and differences between magnetic refrigeration and current commercial refrigerators, which rely on vapor compression.

Vapor compression utilizes four main components; an expansion valve, an evaporator, a compressor, and a condenser, as shown in (a) of Figure 2.1. A liquid refrigerant circulates through the entire system to act as a medium for transferring heat to and from the environment. The heat is absorbed into the refrigerant from the refrigerating environment around

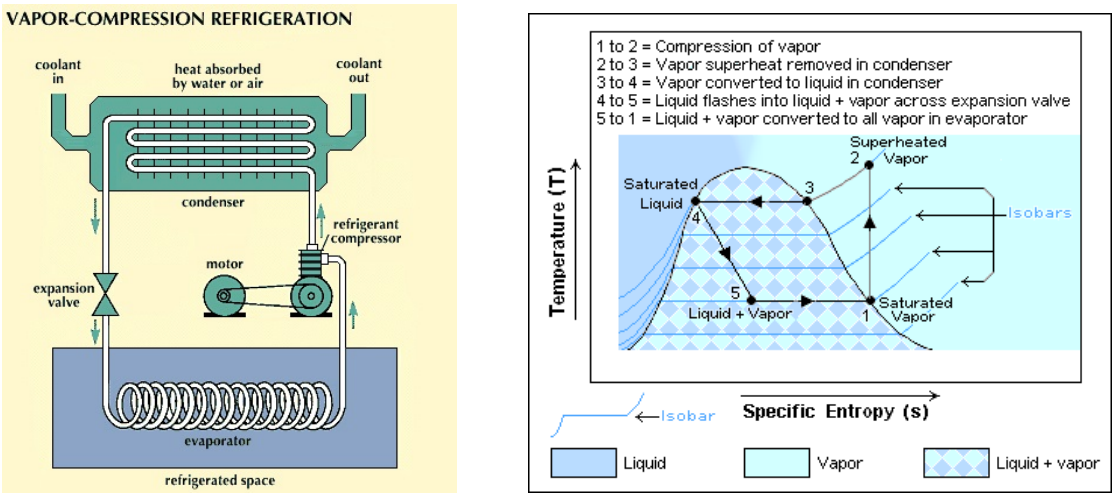

(a) (b)

Figure 2.1: (a) Diagram of vapor compression refrigeration[16]. (b) Specific Entropy-Temperature diagram for vapor compression cycles[17].

the evaporator, changing the refrigerant into a gaseous state. The refrigerant is transported to the condenser, where the heat from the refrigerant is released into a surrounding medium, like air or water. Work is applied to the compressor to prepare the refrigerant vapor for condensation back into a liquid. An Entropy-Temperature diagram of the cycle is shown in (b) of Figure 2.1.

2.3 Thermodynamics of the Magnetocaloric Effect

The MCE describes the relationships among temperature, entropy, and magnetic properties of a material. Usually, it describes how the temperature and entropy of a material change with respect to its magnetization and an applied magnetic field. The MCE can be derived from standard thermodynamic relations applied to magnetic solids in equilibrium[18].

If a ferromagnetic sample is taken to be a thermodynamic system with an externally applied magnetic field, the change in internal energy of the sample can be described using the fundamental thermodynamic relation for magnetic systems as

$$dU = TdS - pdV + \mu_0 HdM \tag{2.1}$$

where U is the internal energy, T is the temperature, S is the entropy, p is the pressure, V is the volume, H is the intensity of the internal magnetic field, and M is the magnetization. Assuming that the change in volume of the system is negligible, dV=0, and the quantities of the system are taken per unit mass, the relation becomes

$$du = Tds + \mu_0 H dm \tag{2.2}$$

The change in specific entropy can be fully determined then by the temperature and magnetic field. A change in specific entropy can be written as

$$ds = \Big(\frac{\partial s}{\partial T}\Big)_H dT + \Big(\frac{\partial s}{\partial H}\Big)_T dH \tag{2.3}$$

Specific entropy can also be written in terms of the variational heat into the closed system of a reversible process δq over the temperature of the system T as

$$ds = \frac{\delta q}{T} \tag{2.4}$$

The specific heat capacity of a material under some parameter x is defined as

$$c_x = \Big(\frac{\delta q}{dT}\Big)_x \tag{2.5}$$

If the magnetic field H is taken to be the parameter held constant for the specific heat, then

$$\frac{c_H}{T} = \Big(\frac{\partial s}{\partial T}\Big)_H \tag{2.6}$$

The relation between entropy, temperature, magnetization, and magnetic field is defined using the Maxwell Relation

$$\Big(\frac{\partial s}{\partial H}\Big)_T = \mu_0 \Big(\frac{\partial m}{\partial T}\Big)_H \tag{2.7}$$

Replacing equations 2.6 and 2.7 into 2.3 gives a new expression for the change in specific entropy

$$ds = \frac{c_H}{T} dT + \mu_0 \Big(\frac{\partial m}{\partial T}\Big)_H \tag{2.8}$$

We are interested in the temperature change of the system under an adiabatic process (ds=0) and a changing magnetic field.

$$dT = -\frac{T}{c_H}\mu_0\Big(\frac{\partial m}{\partial T}\Big)_H \tag{2.9}$$

Finally, integrating over the magnetic field change gives us the adiabatic temperature change ΔT_{ad}

$$\Delta T_{ad} = -\mu_0 \int_{H_i}^{H_f} \frac{T}{c_H}\Big(\frac{\partial m}{\partial T}\Big)_H dH \tag{2.10}$$

It is also possible to calculate the reversible change in entropy starting from equation 2.8. In an isothermal process (dT=0) over a changing magnetic field, the reversible change in entropy is equal to the change in magnetic entropy.

$$ds = \mu_0\Big(\frac{\partial m}{\partial T}\Big)_H \tag{2.11}$$

where, after integrating over the magnetic field, gives Δs.

$$\Delta s = \mu_0 \int_{H_i}^{H_f} \Big(\frac{\partial m}{\partial T}\Big)_H dH \tag{2.12}$$

In both the ΔT_{ad} and Δs expressions, an increase in $\frac{\partial m}{\partial T}$ leads to an increase in both quantities.

Phase transitions can be divided into 2 categories, first and second order transitions. First order transitions demonstrate more abrupt changes than second order transitions, so materials that have first order transitions usually have larger $\frac{\partial m}{\partial T}$ values at their critical temperature. Second order transitions have less abrupt, but still substantive, changes, so they have smaller $\frac{\partial m}{\partial T}$ values compared to first order transitions at the critical temperature. Second order transitions though have a wider operating temperature range because the $\frac{\partial m}{\partial T}$ is more spread out.

2.4 Adiabatic Demagnetization

A magnetic cooling cycle that utilizes the MCE and resembles the vapor compression cycle is based on a process called adiabatic demagnetization refrigeration (ADR). Imagine a

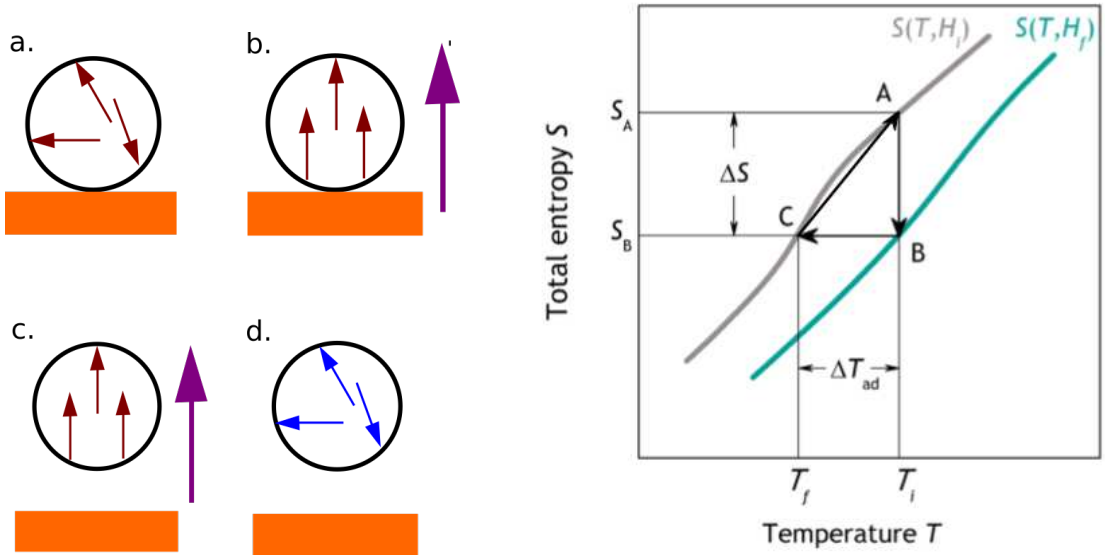

(a) (b)

Figure 2.2: (a) Adiabatic demagnetization refrigeration (ADR) cycle, where the purple arrow is an external magnetic field, the black circle is a magnetic material, and the orange rectangle is a thermal bath at temperature T_i (b) S-T diagram of an ADR cycle. A-B is the AD process and B-C is the isothermal magnetization process[2]. A-C is a process that increases the heat and entropy of the system so that another ADR cycle can be performed.

magnetic material in contact with a thermal bath, as shown in (a) of Figure 2.2. (a.) The magnetic spins of the material are ordered randomly at some initial temperature T_i. In magnetic systems, the entropy of the system increases the more randomly aligned the magnetic spins are, and conversely decreases the more spins are aligned in the same direction. It is energetically favorable for spins to be aligned in the same direction because of the exchange interaction, so energy is required to misalign neighboring spins. (b.) Then, a magnetic field is applied in some direction that aligns the spins, decreasing the entropy and increasing the temperature in the material. This process is called isothermal magnetization (process A-B in (b) of Figure 2.2). Since the material is in contact with a thermal bath, the material's temperature is not raised and the heat generated from the isothermal magnetization process is absorbed into the thermal bath. (c.) The material is separated from the thermal bath while the magnetic field is still applied. (d.) Finally, the magnetic field is decreased and the magnetic spins in the material are allowed to randomize again. As the spins misalign, they absorb energy from the material and decrease the overall temperature of the material as described by the MCE (process B-C in (b) of Figure 2.2). This process is called adiabatic demagnetization and the material arrives at $T_f < T_i$, completing the magnetic cooling cycle. This cycle can be repeated to cool a material if the thermal bath acts as a heat sink without increasing the temperature of the material when the two are brought together again in (a.).

2.5 Research Progress of Magnetocaloric Materials

Many different families of magnetocaloric and giant magnetocaloric materials have been studied extensively over the last few decades[2, 3]. It is difficult to compare MCE materials as there is no agreed upon set of properties within the MCE community, as well as no comprehensive weighting scheme or all-encompassing factor that captures of all their properties. Some families of materials produce higher temperature changes, some families have closer-to-room-temperature phase transition temperatures, and some families are cheaper and easier to produce. A widely used metric for comparing MCE materials is called the relative cooling power (RCP). The RCP is a product of ΔS_{max} and the full-width half max (FWHM) of the

ΔS peak about a prescribed temperature range $\delta T_{FWHM,S}$, or a product of $\Delta T_{ad,max}$ and the FWHM of the ΔT_{ad} peak about a prescribed temperature range $\delta T_{FWHM,T}$, as shown below.

$$RCP_s = |\Delta S_{max}| \delta T_{FWHM,S} \tag{2.13}$$

$$RCP_T = |\Delta T_{ad,max}| \delta T_{FWHM,T} \tag{2.14}$$

Large temperature and entropy changes though are usually the first properties considered, and will be the main focus of this project. There are many other material properties besides ΔS and ΔT_{ad} that must be considered when searching for a magnetic refrigerant material that will be covered in the next section.

Most promising MCE materials require external magnetic field changes greater than 1 T to deliver temperature changes above 2 K, a benchmark temperature change for competitive MCE materials. These materials include Gadolinium (Gd) and Gadolinium alloys, Heusler alloys, manganites, Manganese alloys, and amorphous alloys. Below is a table showcasing a few of these materials and their thermodynamic properties[3].

Material	Family	T_{max} (K)	$H_f(T)$	ΔS_{max} ($\frac{kJ}{m^3 K}$)	ΔT_{ad}^{max} (K)
Single Crystal Gd	Gd	295	2	49	5.2
$Gd_5Si_2Ge_2$	Gd Alloy	277	2	85	5
$LaFe_{11.6}Si_{1.4}$	Lanthanide Alloy	200	2	54	2.2
$MnFeP_{0.45}As_{0.55}$	Manganese Alloy	303	1	82	2.8
$Ni_{50}Mn_{37}Sn_{13}$	Heusler Alloy	295	2	-55	
$La_{0.67}Sr_{0.33}MnO_3$	Manganite	370	2	16.7	1.6
$Fe_{79}B_{12}Cr_8Ce_5$	Amorphous Alloy	295	1.8		1.3

Table 2.1: Properties of Competitive MCE materials from various families of materials. T_{max} is the maximum temperature of the ΔS curve and H_f is the applied magnetic field change from 0 T.

2.6 Material Properties for MCE Refrigeration

There are a host of properties that magnetocaloric materials need to possess in order to be deemed worthy of being used for cooling. Ideally the magnetocaloric material would

possess all of these properties, but that is beyond the scope of the current phase of this project. This is also not an exhaustive or agreed upon list of desired properties. These properties are[18]:

- large temperature difference (ΔT_{ad})
- large entropy difference (ΔS)
- low specific heat and high thermal conductivity
- first order phase transition
- low Debye temperature values
- Phase transition temperature near working temperature
- no thermal or magnetic hysteresis to enable high operating frequency and, consequently, large cooling power*
- non-toxic
- resistant to corrosion
- good mechanical properties
- low manufacturing costs necessary for commercial viability
- low environmental impact
- high electrical resistance in order to avoid Foucault currents in the processes of rapid change in magnetic field.*

*These criteria are not relevant for systems that do not employ external magnetic fields

2.7 Magnetic Anisotropy and Magnetoelastic Couplings

Ferromagnets have a special type of magnetic anisotropy, called magnetocrystalline anisotropy, that correlates to a preferred direction of magnetization, called the "easy axis", or direction of easy magnetization. This property is a by-product of the spin-orbit coupling of electrons within the crystal lattice. The direction of easy magnetization of a crystal is the direction of spontaneous magnetization in the absence of an external magnetic field. The presence of an easy axis makes the direction parallel to the easy axis the most energetically favorable direction the spins can point in. Consequently, the spins require energy to point away from the easy axis. The energy difference between a spin pointing away from the easy axis and the same spin aligned with the easy axis is the (crystal) anisotropic energy of the system.

For a ferromagnet like Nickel, which has a face-centered cubic (FCC) unit cell, the anisotropic energy can be expanded into a series of direction cosines of the form[19]

$$E_{ani} = K_0 + K_1(\alpha_1^2\alpha_2^2 + \alpha_2^2\alpha_3^2 + \alpha_3^2\alpha_1^2) + K_2(\alpha_1^2\alpha_2^2\alpha_3^2) + ... \tag{2.15}$$

where K_i are anisotropy constants and α_i are direction cosines. Since K_0 is usually independent of the direction of magnetization, it is often ignored because we're interested in the change in energy. The series is often cut off at the K_1 or K_2 term as further terms are negligibly small in comparison.

Magnetoelastic couplings within ferromagnets also contribute to a ferromagnets energy and are responsible for another kind of anisotropy. The stress applied on a ferromagnet creates another easy axis in the direction of applied stress, leading to a stress induced anisotropy within the material. If the applied stress induces a volume change in the ferromagnet, then in this setting the stress anisotropy is effectively the same phenomenon as a property known as magnetostriction. Magnetostriction is a magnetoelastic coupling that relates volume changes in ferromagnets to variations in their magnetization. In total, an applied stress can affect the magnetization in ferromagnets. The energy contribution from isotropic stress anisotropy

is

$$E_{me} = \frac{3}{2}\lambda\sigma \sin^2\theta \tag{2.16}$$

where λ is the magnetostriction coefficient, σ is the applied stress on the ferromagnet, and θ is the angle between the magnetization and the applied stress. It is important to note that in the magnetostriction energy term, the squaring of the angle between the magnetization and the stress makes both parallel and anti-parallel states of magnetic spins energetically degenerate. For a ferromagnet undergoing a stress after having been magnetized in some direction, the energy term above would alter the magnetization of the ferromagnet as shown in Figure 2.3. The change in magnetization can be thought of as due to some applied external

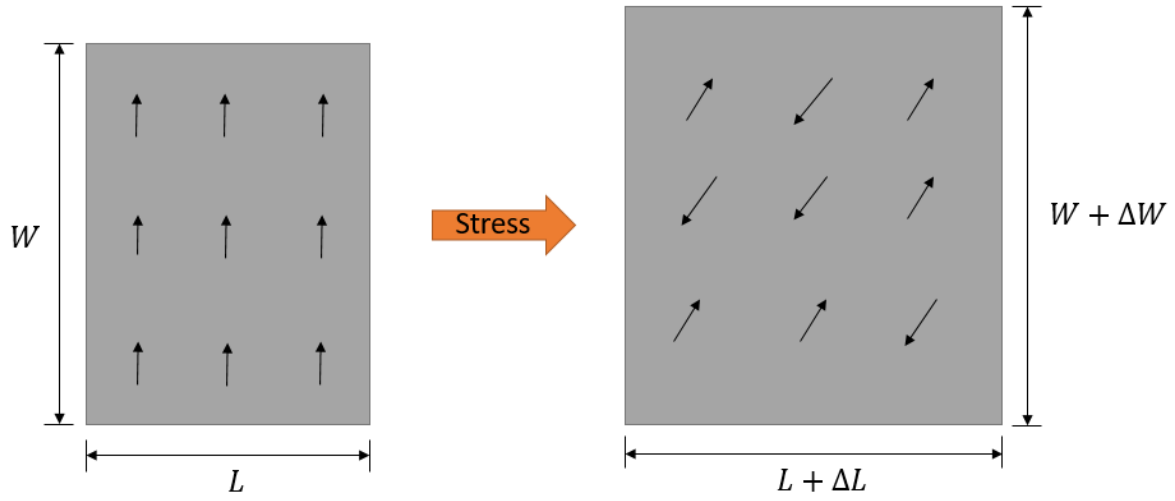

Figure 2.3: Diagram of magnetostriction induced by a stress in a ferromagnet. On the left is a magnetized state of an unstressed ferromagnet. On the right is a stressed ferromagnet with deformations in the x and y directions.

magnetic field. This stress anisotropy field induced in the ferromagnet is described by the relation[5]:

$$H_{K\sigma} = \frac{3\lambda\sigma}{M_s} \tag{2.17}$$

The stress anisotropy field has also been called the coercivity, the coercivity field, or the coercive field.

2.8 Metal-Insulator Transition of Vanadium (IV) Dioxide

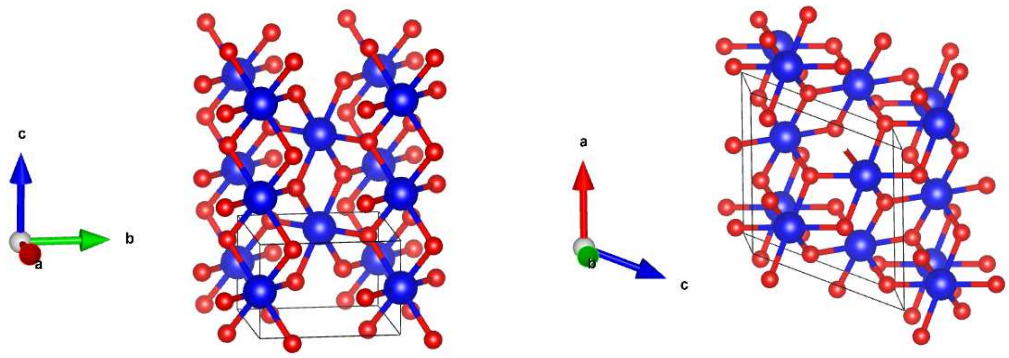

(a) Tetragonal (b) Monoclinic

Figure 2.4: (a) VO_2 in its tetragonal phase and (b) VO_2 in its monoclinic phase.

Vanadium (IV) Dioxide (VO_2) undergoes a Metal-Insulator structural phase transition (MIT) from a high-temperature tetragonal lattice to a low-temperature monoclinic lattice at roughly 340 K, undoped, as shown in Figure 2.4(a) and Figure 2.4(b). The tetragonal structure is conducting and the monoclinic structure is insulating. This first order phase transition can be driven using temperature and voltage.

2.9 VO_2/Ni System

This system in question is a heterostructure with 100 nm of VO_2, deposited non-epitaxially, on a substrate as shown in Figure 2.5. 15 nm of Nickel is deposited on the VO_2. If a large enough voltage is applied across the VO_2, the VO_2 undergoes its MIT and induces a 20-100 MPa stress on the Nickel crystal lattice. Given Nickel's comparatively high magnetostriction coefficient, the large applied stress on the Nickel lattice from the VO_2 translates into a magnetostrictive force that changes the orientations of magnetic spins in the Nickel. This magnetization change within the Nickel that can be used in an ADR cycle. The isothermal

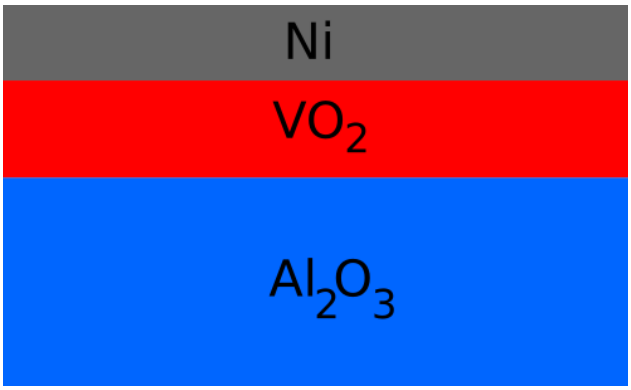

Figure 2.5: Side view of thin film heterostructure on a sapphire substrate

magnetization process is accomplished in the Nickel by either anisotropy alone, or by the addition of a small applied magnetic field to fully magnetize the Nickel, while the applied stress from the VO_2 phase transition would perform the adiabatic demagnetization process. The mechanism for this will be discussed in Chapter 3. If a small magnetic field is used to magnetically saturate Nickel for the isothermal magnetization process, this ADR process would utilize magnetic fields like other MCE materials, except for the fact that the magnitude of the magnetic field needed for magnetizing Nickel is orders of magnitude smaller than the magnitude needed to perform an standard ADR cycle.

2.10 Piezoelectric Effect and PZT

PZT, or Lead Zirconate Titanate, is a piezoelectric material. The piezoelectric effect describes the relationship between electrical and mechanical properties of a material. In this project, the relevant electrical and mechanical properties are voltage and mechanical stress[20]. The electrodes apply a voltage that is converted into a deformation in both the longitudinal and transverse directions non-isotropically. A schematic of the specific PZT film used is shown in Figure 2.6.

2.11 PZT/Ni System

The relevant layers of the PZT system are the PZT itself and the Platinum substrate, as shown in Figure 2.8. 15 nm of Nickel is deposited on the PZT. For the PZT/Ni system, leads

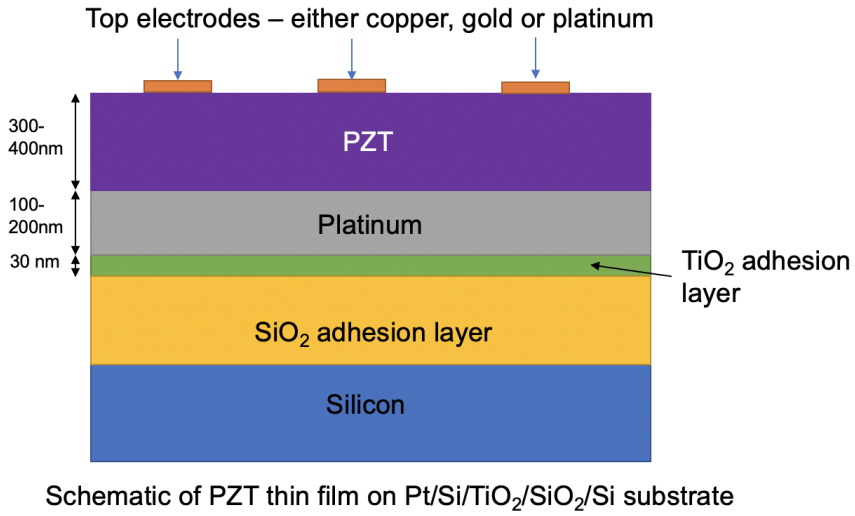

Figure 2.6: Schematic of the entire PZT film.

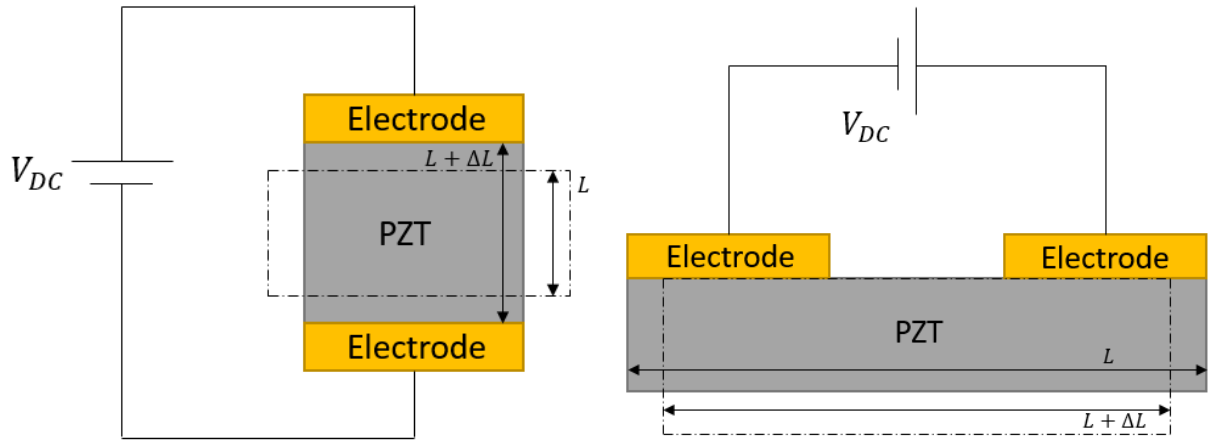

(a) (b)

Figure 2.7: Diagrams of (a) standard positioning of electrodes on a piezoelectric like PZT, and (b) surface positioning of electrodes on a piezoelectric.

are positioned on the PZT next to the Nickel bar. The leads are both on top of the PZT as shown in Figure 2.7 (b), rather then on opposite sides of the PZT as shown in Figure 2.7 (a). This is done in order to induce a deformation parallel to the surface of the PZT to act in a similar manner to the VO_2 structural phase transition. The stress induced by the PZT deformation in the Nickel has not been measured unlike that of the Nickel on the VO_2.

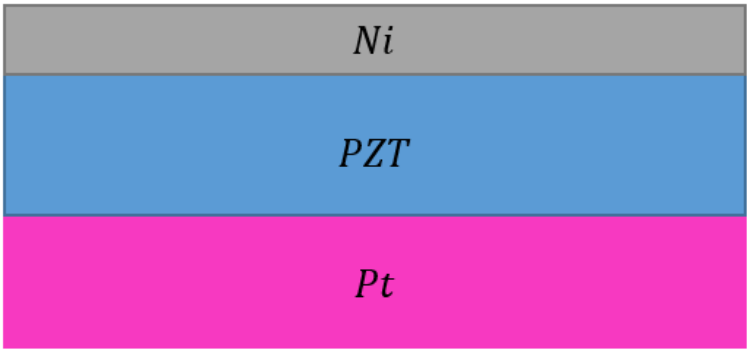

Figure 2.8: PZT/Ni system on a Platinum substrate.

CHAPTER 3

SIMULATING THE MAGNETOCALORIC EFFECT IN NICKEL HYBRID SYSTEMS

3.1 Molecular Dynamics Simulation

3.1.1 Theoretical Model

A molecular dynamics (MD) simulation was created using the MD software LAMMPS[21] to predict the stress profile within the Nickel due to the structural phase transition of VO_2. There are many assumptions used in this preliminary model, but there are still useful results that can be gathered from these simple simulations. It is assumed that the phase transition is instantaneous.

The overall procedure is as follows. First, a bilayered system is initialized in LAMMPS with FCC Nickel on top of VO_2 in its tetragonal form, both aligned in the <100> plane with periodic boundary conditions in the x, y, and z directions for Figure 3.2, Figure 3.3, Figure 3.4, and Figure 3.5. This was done because the force fields used for the VO_2 are for a bulk sample. Figure 3.6 also had periodic boundary conditions on x and y, while a non-periodic "shrink wrap" boundary was taken for the z direction. This was done in order to mimic the relatively infinite size of the xy plane of the thin film to that of its thickness in the z direction. A canonical ensemble, or NVT, is chosen for these simulations. There are Nickel, Vanadium, and Oxygen atoms in the system. The system is optimized at 300 K to find the lowest energy structure, where properties of the system are recorded every 10 time steps. 1 time step is 1 femtosecond. The simulation terminates after 5000 time steps, or if the change in energy of the system is less then 10^{-15} energy units of the LAMMPS "metal" unit system (the equilibration criteria). The stresses are calculated for each atom. Another separate system is initialized with Nickel on top of VO_2 in its monoclinic form. The systems are optimized and the stresses are also calculated for each atom. Then, discrete layers in the direction perpendicular to the interface are defined, as shown in Figure 3.1, and

an average stress per atom is calculated for each layer. Each layer is about 1.76 Angstroms (Å) apart, which is half the unit cell size of Nickel. This is done in both VO_2 structures. The difference between the average stress in one layer in the tetragonal system and the same layer in the monoclinic system is taken to be the stress induced in the Nickel by the VO_2 phase transition. The same procedure was carried out at 400 K, but the output was identical to the output at 300 K.

In LAMMPS, the force fields chosen for various molecular interactions are listed in the table below. The coefficients used in the Morse and Buckingham potentials are listed in Appendix Table A.1.

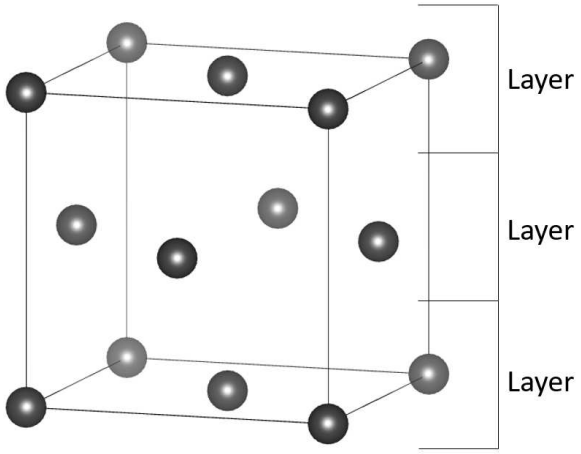

Figure 3.1: Nickel FCC unit cell discretized into layers for average stress calculations.

Atoms	Force Field/IAP
Ni-Ni	MEAM for Ni[22]
Ni-V	MEAM for VNiTi[23]
Ni-O	MEAM for NiAlO[24]
V-V	Morse
V-O	Buckingham
O-O	Buckingham

Table 3.1: Force fields and interatomic potentials (IAP) chosen for each atomic interaction.

The LAMMPS input files for the non-periodic case for the VO_2/Ni with the VO_2 in its monoclinic form and its tetragonal form are in Appendix B.

3.1.2 Results and Discussion

The results of the VO_2/Ni simulations are given below. Since the actual total number of atoms of the two thin films is too large for the simulation to run in a reasonable amount of time, smaller geometries of the two thin films were tested instead to capture qualitative and quantitative information. They equilibrated after 10 to 40 time steps depending on the geometry. On the left of the figures are a 2D side-view of the Nickel (grey) and VO_2 (red) geometry, where A is Angstroms. The geometries are a rectangular prism with a square cross section in the xy plane (for example, in Figure 3.2 the length and width of the prism is 63 Å). On the right of the figures are a plot of the calculated average stress per layer of Nickel atoms. The average stresses are calculated from values taken at the end of a series of 10 time steps, not a time average. 1 is the closest layer to the depicted interface on the cross sections.

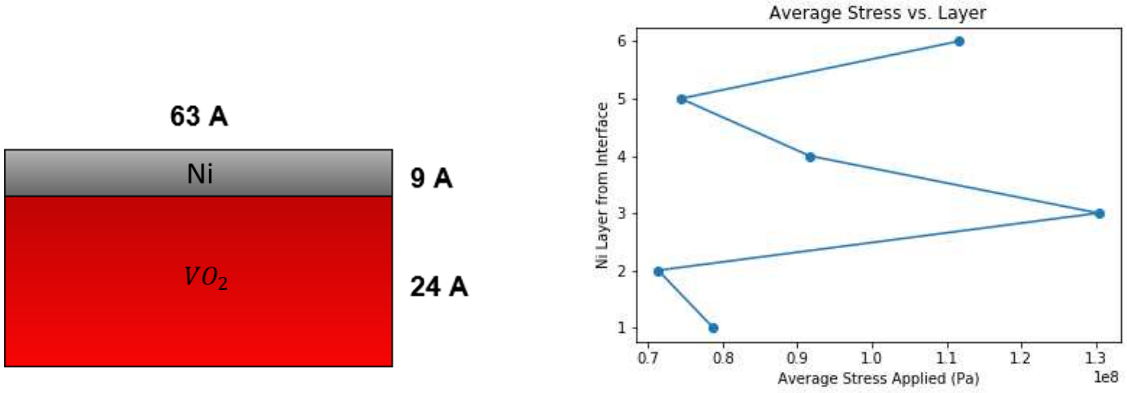

(a) (b)

Figure 3.2: (Left) Diagram of a cross section of a VO_2/Ni bilayer system. (Right) Graph of layers of Nickel away from the interface vs. average stress.

The maximum total stress applied over all geometries is consistently within an order of magnitude of that obtained from experiment of pure VO_2 with no Nickel, about 100 MPa,

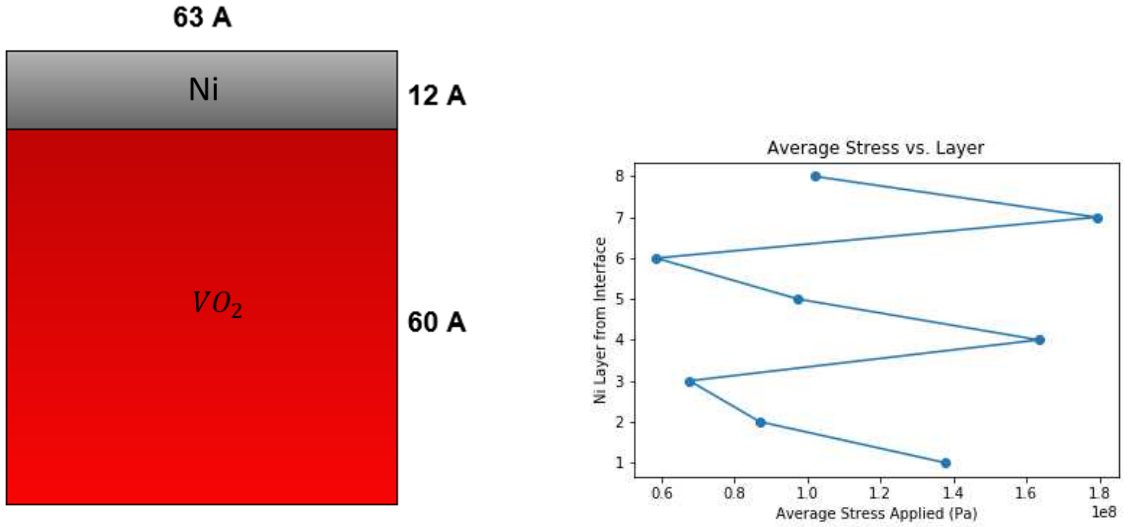

(a) (b)

Figure 3.3: (Left) Diagram of a cross section of a VO_2/Ni bilayer system. (Right) Graph of layers of Nickel away from the interface vs. average stress.

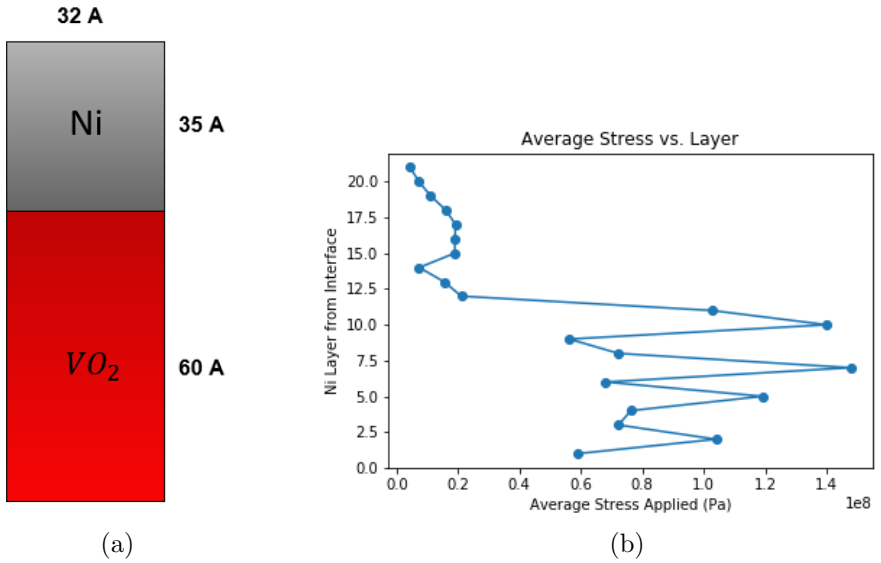

(a) (b)

Figure 3.4: (Left) Diagram of a cross section of a VO_2/Ni bilayer system. (Right) Graph of layers of Nickel away from the interface vs. average stress.

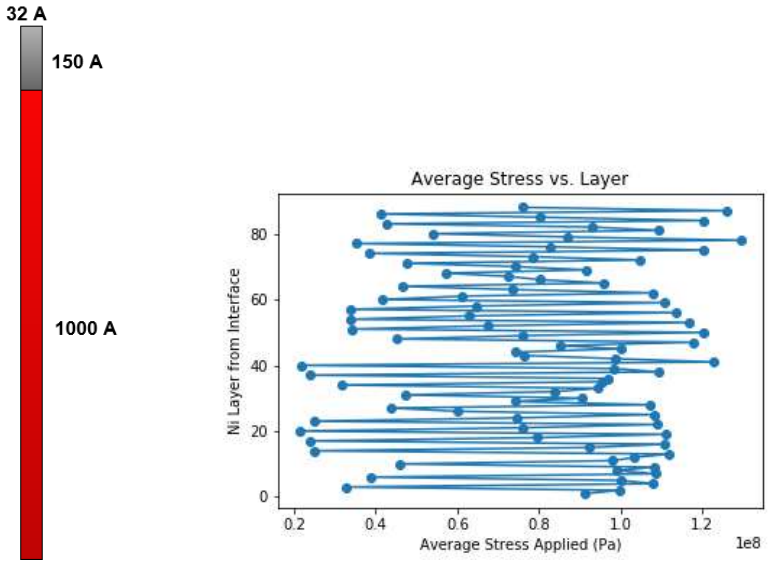

(a) (b)

Figure 3.5: (Left) Diagram of a cross section of a VO_2/Ni bilayer system. (Right) Graph of layers of Nickel away from the interface vs. average stress.

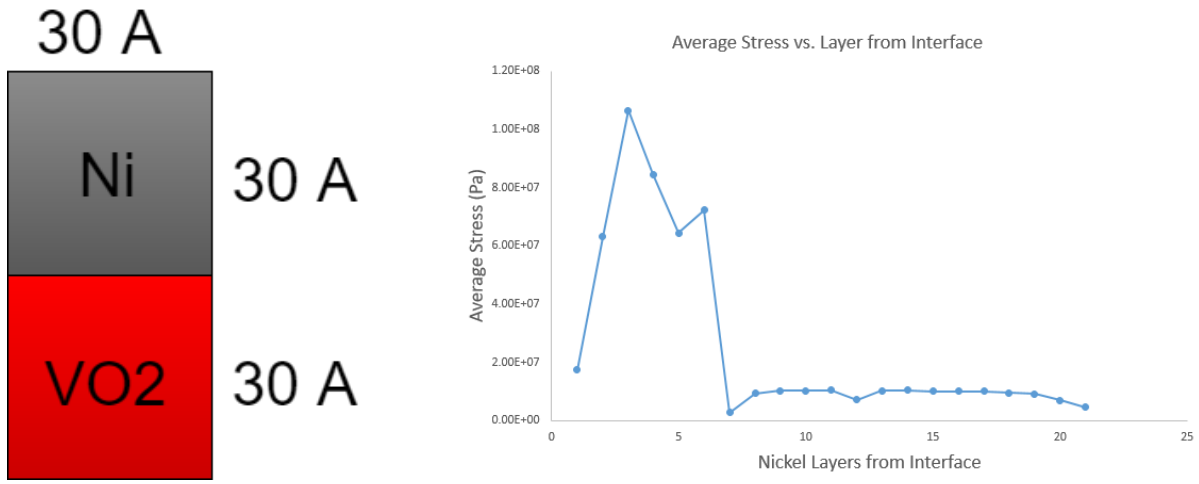

(a) (b)

Figure 3.6: (Left) Diagram of a cross section of a VO_2/Ni bilayer system. (Right) Graph of layers of Nickel away from the interface vs. average stress.

or 1e8 Pa. The average stress after the spike in Figure 3.6 is about 1e6 Pa, which is the same order of magnitude as that measured in the VO_2/Ni system here[5]. The oscillations in the first four simulations with all periodic boundary conditions have oscillations potentiallyt because the Nickel layer has a top and a bottom interface with the VO_2 layer. The systems were run at 300 and at 400 K, but each had identical stress values in both temperatures at each layer, indicating that at least one of the assumptions made for the simulation does not capture the temperature dependence of the VO_2 phase transition, only the structural difference.

3.2 Monte Carlo Simulation

3.2.1 Theoretical Model

The thermodynamic and magnetic properties of the Nickel are simulated using a Monte Carlo simulation. This simulation has no preference on what material the Nickel is on, only that the material induces a stress in the Nickel. A perfectly isotropic simple cubic lattice is assumed (shown in Figure 3.7(a)), rather than a face centered cubic (FCC) lattice (shown in Figure 3.7(b)). This was done for improving computational efficiency at the cost of decreasing accuracy in the results. Operations performed on a cubic array (which has the same configuration as a simple cubic lattice) are much faster than accounting for specific distances and positions of atoms in standard MD simulations and performing calculations. (At the start of this project LAMMPS did not have a magnetic spins package). The Hamiltonian of the bulk crystalline Nickel is based on the classical Heisenberg-like model with nearest neighbor interactions and a cubic anisotropy term as given below[25]:

$$H_{ex} = -J \sum_{i \neq j}^{N} s_i \cdot s_j \tag{3.1}$$

$$H_{ani} = -K \sum_{i}^{N} \alpha_x^2 \alpha_y^2 + \alpha_y^2 \alpha_z^2 + \alpha_x^2 \alpha_z^2 \tag{3.2}$$

$$H_{mag} = -g\mu_b \sum_{i}^{N} s_i \cdot h_{ext} \tag{3.3}$$

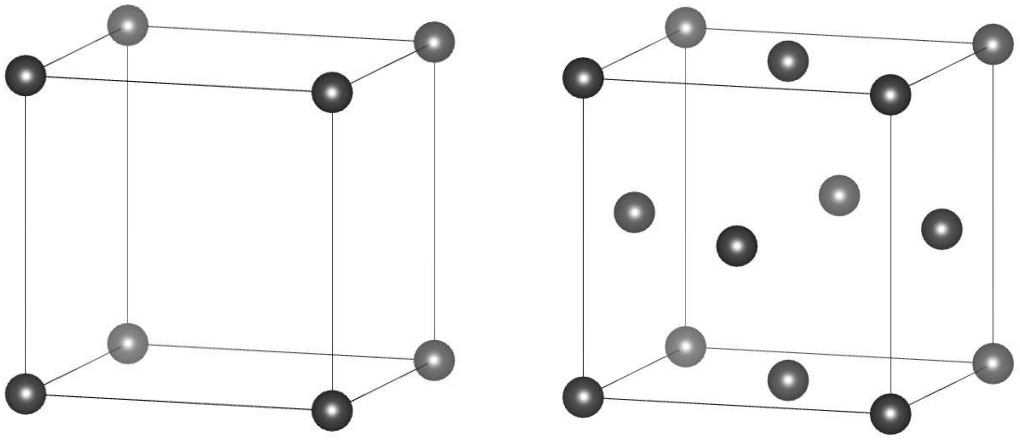

(a) (b)

Figure 3.7: (a) A simple cubic and (b) FCC lattice.

$$H_{base} = H_{ex} + H_{ani} + H_{mag} \tag{3.4}$$

The first term in this expression is the exchange interaction between neighboring Nickel atoms. The sum runs over every site in the lattice i and their nearest neighbor sites j. The second term is the cubic anisotropy interaction where the sum is over all sites i. The third term is the external magnetic field interaction over all sites. In this 3D case s is of unit length and the α_i are the direction cosines of the site spins with the easy axis of Nickel. g is the Lande factor, and μ_b is the Bohr magneton. J is the exchange interaction coefficient for bulk Nickel and K is the cubic anisotropy constant for bulk Nickel as given below[26].

$$J = \frac{3k_bT_c}{\epsilon z} \tag{3.5}$$

$$K = \frac{k_u a^3}{n_{at}} \tag{3.6}$$

Where k_b is Boltzmann's constant, T_c is the Curie temperature, ϵ is a correction factor for spin waves, taken to be 1 to ignore spin wave interactions, z is the number of nearest neighbors taken to be 6 for a simple cubic lattice, k_u is the cubic anisotropy constant, a is the unit cell size, and n_{at} is the number of atoms in a cell. The cubic anisotropy term is

expressed with one anisotropy constant instead of the two known Nickel anisotropy constants so that the simpler (111) easy axis can be used rather than a more computationally intensive linear combination.

The final Hamiltonian that is analyzed includes the contribution to the energy from the VO_2 phase transition or PZT piezoelectric deformation. This final term is based on the assumption that the contribution to the energy is manifested through a magnetostrictive (str) interaction as shown below[25].

$$H_{str} = -\frac{3a^3}{2}\sigma\lambda sin^2(\theta) \tag{3.7}$$

where σ is the lattice strain in the Nickel, λ is the magnetostrictive coefficient of Nickel, taken to be $-34 * 10^{-6}$[5], and θ is the angle between the magnetization of the Nickel and the lattice strain, assumed to be in the XY plane (coplanar with the thin film). This term is a correction for the anisotropy term when an external stress causes a torque on the magnetic spins to point away from the easy axis. The total Hamiltonian looks like:

$$H_{tot} = H_{ex} + H_{ani} + H_{mag} + H_{str} \tag{3.8}$$

In this model the strain is assumed to be uniform throughout the lattice, even though it is apparent that, for this system in particular, the lattice strain should be greatest near the interface and decrease as the distance from the interface increases (as can be seen in the previous section). This is the simplest model Hamiltonian considered. More complicated Hamiltonians will be considered in the future if the proposed simple model is not sufficient in describing the thermodynamic properties of the Nickel obtained in future measurements.

3.2.2 Monte Carlo Metropolis-Hastings

A cubic lattice is created where each lattice site is randomly assigned a state from a list of available spin states. This randomly assigned start is considered a "hot start" because at higher temperatures there is a greater probability that neighboring spins will not be in the

same spin state. Conversely, a "cold start" has all lattice sites in the lattice created with the same spin state.

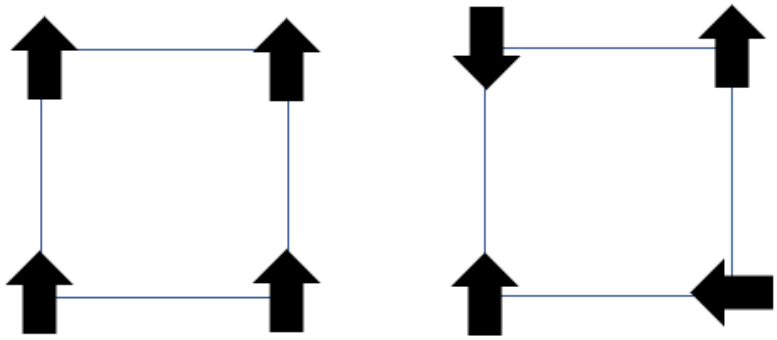

Figure 3.8: Diagram of a (Left) Cold start and a (Right) Hot start in 2D for the Monte Carlo simulation.

A standard Metropolis-Hastings (MH) algorithm with periodic boundary conditions is employed where random single spin flip attempts are made in the lattice. If the spin flips reduce the energy of the lattice then the spins are accepted. If they increase the energy of the lattice, then a random number between 0 and 1 is called. If the random number is less then $e^{\frac{-\Delta E}{k_b T}}$ then the spin flip is still accepted. If not, then it is rejected. Computing a number of spin flips on the order of the number of nodes in the lattice is one Monte Carlo Step (MCS). Each set of parameters is run 5 times with 10^2 Monte Carlo steps. On a single CPU this takes about 100 seconds. There is a designated number of "thermalization" steps N_T computed before a chosen number of "measurement" steps N_M are run to allow the system to thermalize before measuring the system. The combination of the electron spin magnetic moment, nuclear spin magnetic moment, and electron angular momentum contribute to the atomic spin pointing in any direction in 3-space on a unit sphere. For computational purposes the unit sphere is discretized into 26 equally probable states and randomly selected at each spin flip.

The thermodynamic quantities energy (E), magnetization (M), magnetic specific heat capacity (C_{mag}), and magnetic entropy (S_{mag}), of the system are calculated using the methods described in the next section [27]. These quantities are calculated in a non-dimensionalized prescription per atomic site to increase computational efficiency.

3.2.3 Thermodynamic Calculations

The four quantities mentioned above are calculated in the manner shown below.[27–29] Here, N_L is the total number of sites in the lattice. N_M is the number of measurement steps. N_T is the number of steps used to thermalize the system. Each quantity is calculated per site in the lattice. $\mathcal{H}$ is the Hamiltonian of the system, H is the magnetic field inside of a material, and brackets around a quantity indicate an expectation value of that quantity.

$$\left\langle \mathcal{H}_{site} \right\rangle = \frac{1}{N_L} \sum_{i}^{N_L} E_i \tag{3.9}$$

The first equation is the expectation value of the Hamiltonian of the system. It is the sum of all site energies in the lattice, averaged over the number of lattice sites, to arrive at the average energy per site.

$$E_{site} = \frac{1}{N_M} \sum_{i}^{N_M} \left\langle H_{site} \right\rangle_i \tag{3.10}$$

The next equation is for the average energy per site of the lattice over the number of measurement Monte Carlo steps. This is like taking a time average of an already spatially averaged system, only instead of time it is the number of Monte Carlo steps. Even though the system is evaluated with $N_M + N_T$ steps, we are only interested in the state of the system after it thermalizes.

$$\left\langle S_{site} \right\rangle = \frac{1}{N_L} \sum_{i}^{N_L} s_i \tag{3.11}$$

This equation is used to determine the expectation value of the magnetization S per lattice configuration. Each site has some magnetization/spin s_i that is summed with all of the other

site spins to calculate the total average magnetization.

$$M_{site} = \frac{1}{N_M} \sum_{i}^{N_M} \left\langle S_{site} \right\rangle_i \tag{3.12}$$

This equation is used to calculate the average magnetization for the measurement steps like the equation for E.

$$c_{mag} = \frac{\left\langle E_{site}^2 \right\rangle - \left\langle E_{site} \right\rangle^2}{k_b T} \tag{3.13}$$

This equation calculates the specific heat of the lattice configuration per site from the difference between variations of squared energy divided by Boltzmann's constant k_b and temperature of the system T.

$$C_{mag} = \frac{1}{N_M} \sum_{i}^{N_M} \left\langle c_{mag} \right\rangle_i \tag{3.14}$$

This equation calculates the average magnetic specific heat per site over all of the measurement lattice configurations.

$$\Delta S_m = \int_0^{H_f} \left(\frac{\partial M}{\partial T} \right)_H dH \tag{3.15}$$

This equation is used to evaluate the change in magnetic specific heat from changes in magnetization with respect to temperature. H_f is the maximum applied field for a given set of parameters. Since integrals are a continuous operation, the change in magnetic entropy ΔS_m is calculated using the approximation[29]:

$$\Delta S_m \left(\frac{T_1 + T_2}{2} \right) = \frac{1}{T_2 - T_1} \left[\int_0^{H_f} M(T_2, H)\, \mathrm{d}H - \int_0^{H_f} M(T_1, H)\, \mathrm{d}H \right] \tag{3.16}$$

where H is the applied magnetic field and H_f is the maximum applied field. This approximation has been discretized again to yield

$$\Delta S_m \left(\frac{T_1 + T_2}{2} \right) \sim \frac{1}{T_2 - T_1} \left[\sum_{i=0}^{N_H - 1} \left(M(T_2, H_{i+1}) - M(T_2, H_i) \right) \Delta H - \sum_{i=0}^{N_H - 1} \left(M(T_1, H_{i+1}) - M(T_1, H_i) \right) \Delta H \right]$$

where ΔH is the field step size and N_H is the number of fields calculated between 0 and H_f. The values of ΔS_m that correspond to T_1 and T_2 for example are then interpolated.

For conditions where an external magnetic field is applied but no stress is applied to the Nickel lattice, H is just the resulting field. For conditions that have applied stress, H is taken to be the stress anisotropy field:

$$H_c = \frac{3\lambda\sigma}{M_s} \tag{3.17}$$

where M_s is the saturation magnetization. If both external magnetic field and stress are applied, then H is the summation of both fields. Finally, the adiabatic temperature change is calculated as shown below. This form

$$\Delta T_{ad} = -T\frac{\Delta S_m}{C_{mag}} \tag{3.18}$$

3.2.4 Results and Discussion

One of the trade-offs between building simulations from scratch and using someone's software is that you understand and have control over the physics in the programs you write from scratch much better then if you were to use someone's software and try and figure out the physics they are employing in their simulations. Unfortunately, this usually means that your from-scratch program runs much slower than someone's software, whether it is because of their algorithms or the languages they used. The greatest limitation of this Monte Carlo simulation is that it is too inefficient to accurately simulate the VO_2/Ni system with appropriate parameters in a reasonable amount of time given the computational resources at my disposal.

More MCS on the order of 10^5 or greater as well as larger system sizes are needed in future runs to be able to simulate the specific system so that the uncertainty of the simulation is minimized. Instead, simulations are run at extremes to identify trends in the model. The trends seen in the simulation match what is expected in magnetocaloric simulations[28, 29]. Increasing the number of atoms (the system size) sharpens the descent in the magnetization

curve around the Curie temperature and lowers the minimum of the magnetization, as seen in (b) of Figure 3.9. Increasing the system size drastically increases computation time though, so all simulations following Figure 3.9 are run with 27 atoms (3x3x3) with 100 thermalization MCS and 100 measurement MCS, from T=.1 to T=4 every .1 T (40 temperatures per run). As mentioned earlier, this takes about 100 seconds. This is an area that could be improved upon in the future with more computational , as increasing the dimension, MCS, or T step size drastically increases computation time. The oscillations in the magnetic field components in the following plots are potentially due to the small simulation size and MCS size.

Applying magnetic and stress fields to the system produces consistent results. The magnetic field points in the +z direction, while the stress is applied in the (+x,+y) direction, or across the diagonal of the thin film. The stress was chosen to be in this direction rather than just (+x) or (+y) to account for the non-isotropic unit cell lattice parameter changes in the VO_2 phase transition, as well as the longitudinal and transverse piezoelectric deformations in the PZT. It is also parallel to the easy axis of Nickel in a 2d system. As the magnetic field strength increases, the amount of thermal energy needed to misalign a spin increases. At the same temperature with the same amount of thermal energy, more spins will stay aligned the stronger the magnetic field, as seen in Figure 3.10. The magnetic field makes the +z and -z states the most energetically favorable, so the magnitude of the magnetization in the z direction increases with applied magnetic fields while the magnitude in the x and y directions decrease. A similar feature can be seen in Figure 3.11. The difference between the magnetic field and the stress field is that the magnetic field pointing in the z direction has one lowest directional energy state parallel to the z axis, while the stress field pointing in the (+x,+y) direction has more than one directional lowest energy state, decreasing the overall magnetization as it is distributed in the xy plane. The magnitude of the magnetization in the x and y directions with large stresses is much larger at higher temperatures then with smaller stresses. (The magnetizations in the x, y, and z directions under different magnetic fields and stresses can be found in Appendix C.) This means that the magnetostrictive force

in its current form can be used to perform the adiabatic demagnetization process of the ADR cycle because it scrambles the direction of the spins and increases the entropy of the magnetic system. If the magnetostriction term's form is chosen so that there is only one lowest energy spin state, say if a non-isotropic form has this behavior, then magnetostriction could also be used to drive the isothermal magnetization process.

Above the Curie temperature, the magnetization should be zero, which has been shown in experiment for ferromagnetic materials including Nickel[30]. However, because the number of atoms used in the simulation are small compared to a bulk system, the magnetization does not reach zero above the Curie temperature. This artifact of simulating small systems leads to ΔS_m and ΔT_{ad} being orders of magnitude greater above the Curie temperature then it should be in practice. In fact, it is orders of magnitude greater than at the Curie temperature, which in experiment the largest temperature and magnetic entropy changes are at the Curie temperature. For this reason the ΔS_m and ΔT_{ad} plots are not included in this section, but can be found in Appendix D.

Overall, by combining the stress profile results of the MD simulation and the magnetization results from applied stress in the MC simulations, one can determine how the phase transition of the VO_2 affects the magnetization of Nickel. It appears that the MD results are consistent in orders of magnitude with experiment, but a reduction in number of assumptions used to simplify the problem would benefit the accuracy of the simulation. The MC simulation appears to follow the correct trends, although the results are very noisy. The MC simulation requires larger system sizes, as mentioned above. Combining both simulations would be beneficial now that a package exists in LAMMPS to include magnetic spin dynamics. It is possible that further effects, like electrocaloric, elastocaloric, magnetoelectric, and others may need to be included in future simulations.

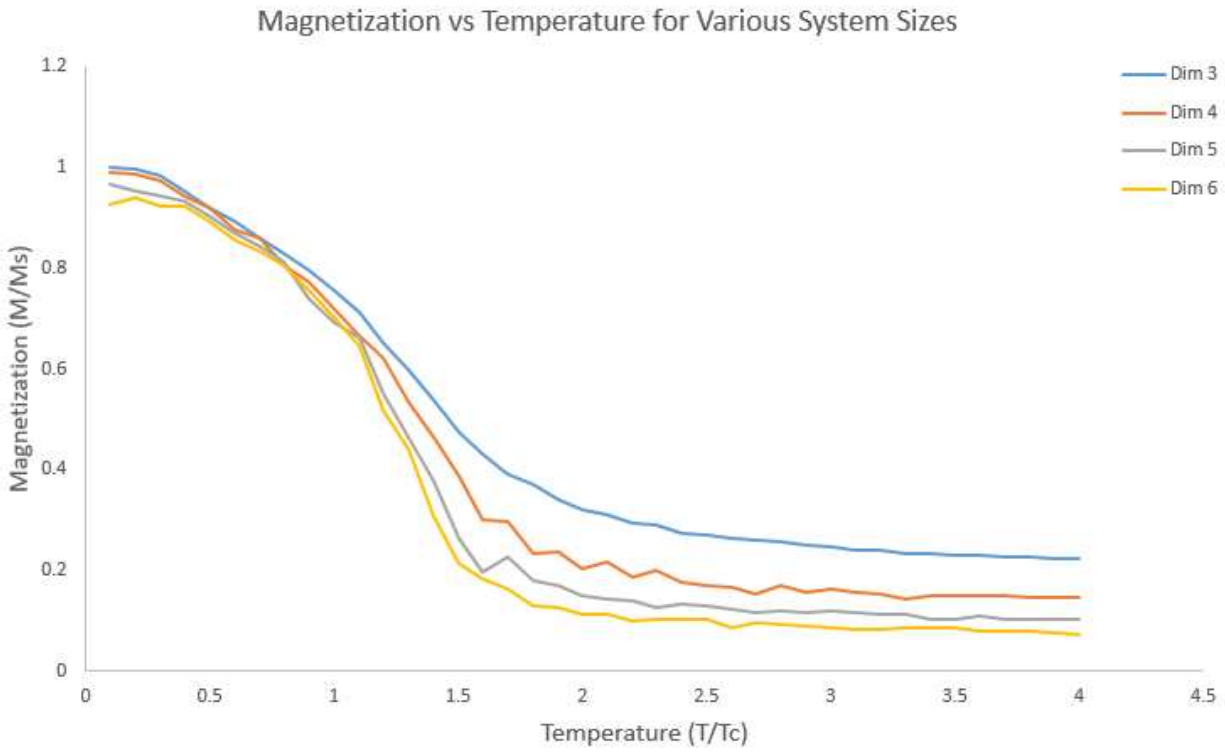

Figure 3.9: Plots of non-dimensionalized magnetization versus non-dimensionalized temperature of a system with no applied fields. "Dim" stands for dimension, which is the number of atoms (system size) in one of the three directions x, y, and z. Magnetization is plotted for 3,4,5, and 6 dimensional systems (27, 64, 125, and 216 atoms total).

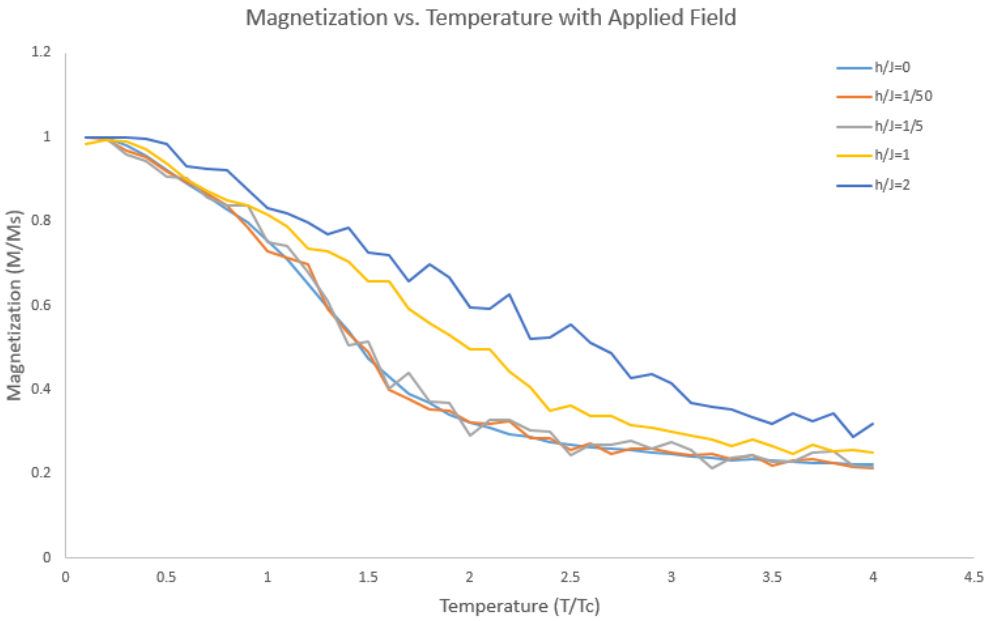

Figure 3.10: Magnetization versus temperature of a dim 3 system with applied magnetic fields of various strengths. Magnetic field strengths are listed as ratios of magnetic field over the exchange interaction constant (h/J).

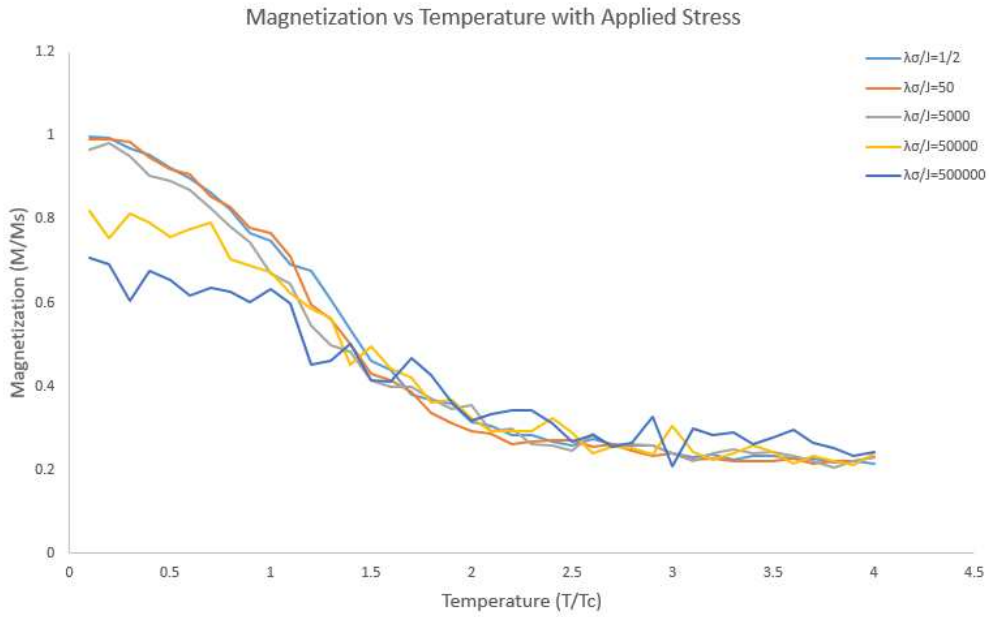

Figure 3.11: Magnetization vs temperature of a dim 3 system with various applied stress strengths. Stress strengths are given as ratios of the magnetostriction coefficient times the stress over the exchange interaction constant ($\lambda\sigma$/J)

CHAPTER 4

EXPERIMENTAL METHODS AND PROCEDURES

4.1 Resistive Thermometry

Resistive thermometry is a technique used for measuring temperature in high resolution situations. This technique is based on an accurate knowledge of the thermometry material's resistance/temperature relationship. To find this relationship, another (primary) thermometer must be used for discerning the resistance/temperature relationship of the thermometry material. This makes the resistive thermometer a secondary thermometer as its calibration depends on the accuracy of the primary thermometer. Resistive thermometry is most commonly used to determine absolute temperature, but for this project we are interested in changes in temperature. By measuring changes in temperature instead of absolute temperature, a greater resolution can be achieved. Changes in temperature are extracted from measuring changes in voltage across the thermometry material and dividing by the current to find the resistance (Ohm's law). Voltage is measured across the thermometry material, in this case a thin film, using a four-point probe, while a constant current is applied. Four leads are connected onto the material surface in a straight line. All leads are equally spaced apart and centered on the thin film. The two outer leads apply and ground a current so that the two inner leads can measure a voltage drop across the material. Since the current is known and the voltage is measured, the resistance can be extracted if needed. For thin films it is not the resistance that is measured, but the sheet resistance. The sheet resistance R_s is calculated almost the same way as actual resistance with Ohm's law, but with an additional correction factor (in this case 4.53 for rectangular samples) based on the thin film's geometry[31].

$$R_s = 4.53\frac{\Delta V}{I} \tag{4.1}$$

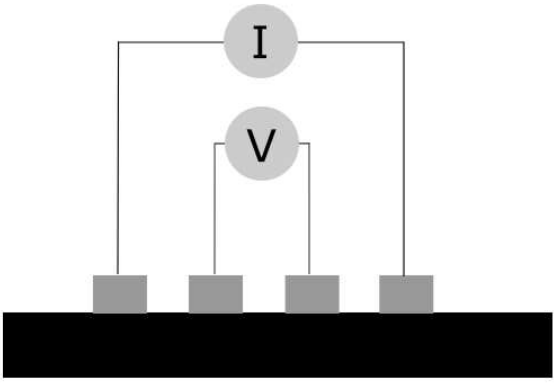

Figure 4.1: Diagram of a four point probe measurement on a thin film surface. I is a current source and V is a voltmeter.

Where ΔV is the voltage drop across the material. The bulk resistivity ρ of the material is obtained by multiplying the sheet resistance by the thin film thickness t.

$$\rho = R_s * t \tag{4.2}$$

The actual resistance is then calculated using the resistivity, length L, and cross section A.

$$R = \rho \frac{L}{A} \tag{4.3}$$

4.2 Lock-In Amplification

For high-resolution measurements, standard nano-volt meters are too noisy. Instead, a lock-in amplifier is used to reduce the noise of the measurement by applying an AC signal and measuring the responses of the system with the same frequency as the AC signal. Because the signal medium is so thin (a 10-100 nm thin film), skin depth effects from the AC signals can be ignored.

The lock-in amplifier generates its own reference signal at a given frequency as[32]

$$V_{ref} sin(\omega_{ref} t + \theta_{ref}) \tag{4.4}$$

The signal waveform that is measured is

$$V_{sig}sin(\omega_{sig}t + \theta_{sig}) \tag{4.5}$$

Within the lock-in amplifier is a phase-sensitive detector (PSD) that multiplies the two sine waves together into

$$V_{psd} = V_{sig}V_{ref}sin(\omega_{sig}t + \theta_{sig})sin(\omega_{ref}t + \theta_{ref} \tag{4.6}$$

Applying the trigonometric identity

$$sin(x)sin(y) = \frac{1}{2}(cos(x - y) - cos(x + y)) \tag{4.7}$$

gives

$$\frac{1}{2}V_{sig}V_{ref}(cos([\omega_{sig} - \omega_{ref}]t + \theta_{sig} - \theta ref) - cos([\omega_{sig} + \omega_{ref}]t + \theta_{sig} + \theta ref)) \tag{4.8}$$

When these two AC signals are passed through a low-pass filter, they are filtered out, unless $\omega_{sig} = \omega_{ref}$. If the signal and reference frequencies are equal, a DC signal is measured in the form

$$V_{psd} = \frac{1}{2}V_{sig}V_{ref}cos(\theta_{sig} - \theta ref) \tag{4.9}$$

As the name suggests, the lock-in amplifier only measures signals of the chosen reference frequency while all other noise with different frequencies is filtered out. The original signal is then extracted from the processed DC signal.

4.3 Sample Preparation

VO_2 films grown in the manner depicted here[5] from collaborators at CSU. The PZT films were grown in the manner depicted here[33] from collaborators at CSM. The PZT thin film was modified as follows. The PZT chip and a glass slide were taped over using kapton tape, exposing only a bar 0.6 mm wide across the length of the chip and the glass slide. DC Magnetron sputtering was used to deposit a thin layer of Nickel. The sputtering parameters were chosen to be 100 W power and a pressure on the order of 10^{-7} mbar for 115 seconds.

Ellipsometry from previous calibration runs was used to determine that when the Nickel is sputtered under these conditions for 105-120 seconds, a layer of 12-15 nm is deposited on the films. 12-15 nm of Nickel was chosen to compare to previous work done by collaborators at CSU with VO_2 and Nickel[5, 34].

4.4 Experiment 1: Voltage-Driven Phase Transition of VO_2

The voltage-driven phase transition of VO_2 has been tested on numerous occasions[35, 36], but many material properties of VO_2 (like crystal structure, orientation, oxidation level, temperature...) affect what that voltage threshold is for any given sample. An experiment to determine the number of Volts per meter necessary to drive the phase transition of the VO_2 at room temperature was conducted in order to determine the voltage threshold for our particular samples. VO_2 thin films (one sputtered, one sol-gel) on sapphire substrates with no Nickel deposited on top are placed on a hot plate. Two thin, parallel, equally spaced lines were painted on the VO_2 surface with silver paint, as shown in Figure 4.2.

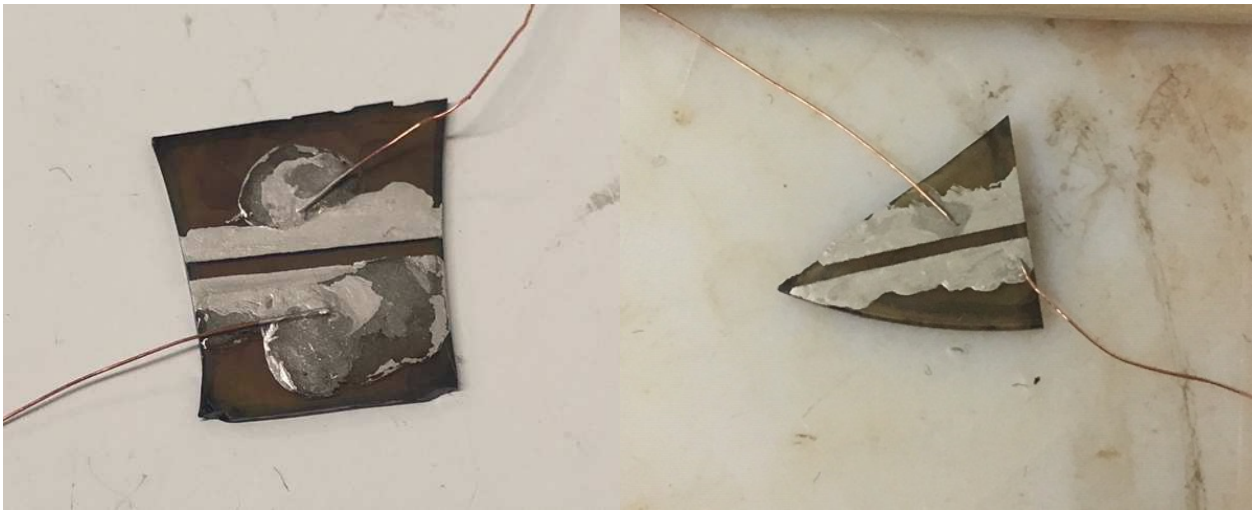

(a) (b)

Figure 4.2: (a) Sputtered VO_2 sample and (b) Sol-gel VO_2 sample with silver paint and copper wire leads.

The distance between the two silver lines is 0.6 mm, and the temperature of the thin films during the measurement was room temperature (22 C or 295 K). A voltage is applied

across the sputtered VO_2 through the silver paint and the current is measured. This is done using a Keithley 2182 Nanovoltmeter. The voltage applied is swept up from 0 to 10 V and then back down to 0 V.

The results of the experiment for the sputtered VO_2 sample are shown in Figure 4.3.

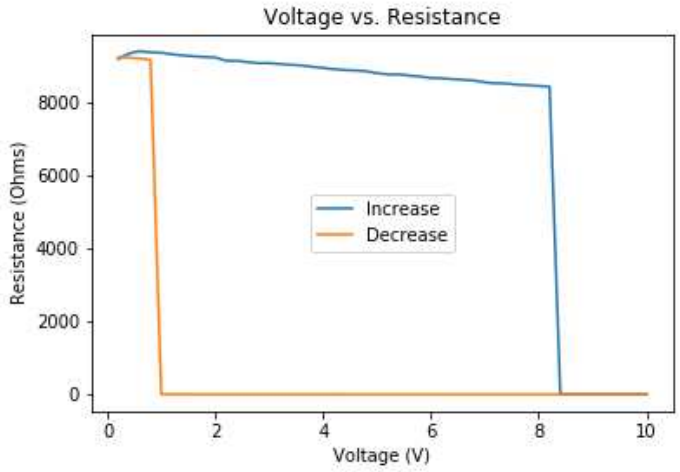

Figure 4.3: Voltage vs. Resistance plot of sputtered VO_2 on sapphire during a voltage sweep from 0 to 10 V. The phase transition occurs at 8.2 V.

The sputtered VO_2 transitions at 8.2 V over a distance of .6 mm. That means the VO_2 in these samples have an average transition voltage of 13.67 V/mm, or 1.367 x 10^4 V/m.

As an aside, we would have continued on with sputtered VO_2 films and performed the experiment in the next section with Nickel on the VO_2, but the sputtered VO_2 films we had had completely oxidized and did not transition anymore when we were performing the temperature measurement. We could not get new sputtered VO_2 films in time, but we were able to get sol-gel VO_2 samples in time. Collaborators informed us that several key material properties were very similar between the sputtered and sol-gel samples, so we decided to see what the voltage threshold was for these films. We did not initially intend to pursue measurements with the sol-gel films until all of our sputtered films had completely oxidized.

The same experiment was conducted with two sol-gel VO_2 thin films. Surprisingly, the sol-gel VO_2 samples did not transition within the 0-10 V range at room temperature like the

sputtered VO_2 samples. The range was increased to 0-20 V, but the samples still did not transition. To make sure the lack of a transition was not a defect in one particular sol-gel film, a second sol-gel film was tested in the same manner and behaved the same way. This experiment was then repeated at higher temperatures until the temperature-induced phase transition of the VO_2 occurred above a hot plate temperature of 65 C. The results of these experiments are shown below for one sol-gel sample.

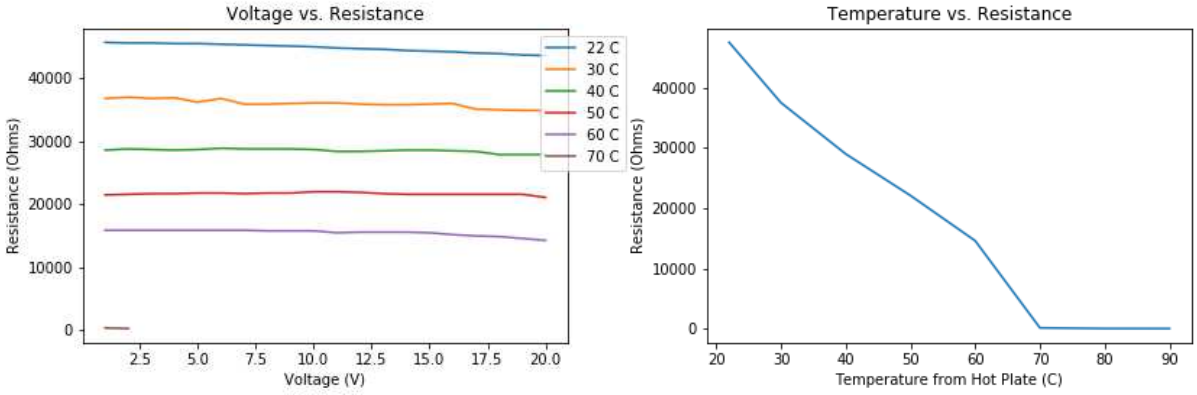

(a) (b)

Figure 4.4: (a) Voltage vs. Resistance plot of sol-gel VO_2 on sapphire during a voltage sweep from 0 to 20 V at various temperatures. (b) Temperature vs. Resistance plot of sol-gel VO_2 on sapphire. The temperature is that read by the hot plate. The phase transition occurs around 65 C.

It appears that the applied voltage did not affect the resistance of the sol-gel VO_2 at all. Either the voltage needed to transition the sol-gel samples needs to be significantly larger than 20 V, or there is some material difference in the VO_2 between the sputtering and sol-gel methods that suppresses a response to voltage in the sol-gel VO_2 completely. In order to determine this, a larger voltage supply would be needed to repeat this experiment, as well as more crystallographic data between the sputtered and sol-gel samples. In light of this result, the temperature measurement is performed with PZT instead of VO_2.

4.5 Experimental 2: Voltage-Induced Temperature Change of PZT/Ni

4.5.1 Nickel Thermometer Calibration

To eventually calibrate the Nickel thermometer, first the error in the equipment used to calibrate it must be determined. A K type thermocouple connected to a Keithley 2182 Nanovoltmeter is used, shown in Figure 4.5. A 15 second measurement with the thermocouple in open air (not connected to the hot plate) is taken to determine the uncertainty in the thermocouple voltage. This 15 second measurement is shown in Figure 4.6. Next, the thermocouple is placed on the hot plate to determine the temperature sensitivity of the thermocouple by taking measurements of the hot plate surface at increasing temperatures. The results for this procedure are shown in Figure 4.7. The uncertainty in the voltage is the amplitude of a 15 second measurement at each temperature and the uncertainty in the temperature is 1 degree C, from the hot plate. The slope of the line, the sensitivity of the thermocouple, is determined to be .0387 mV/K.

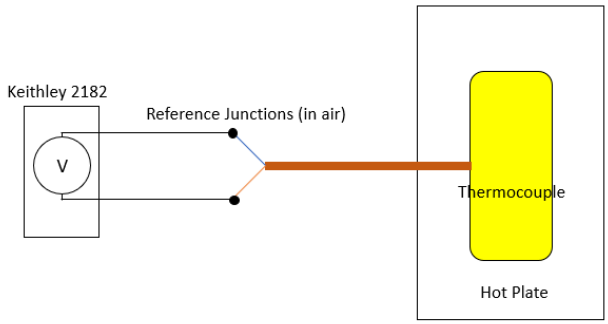

Figure 4.5: Schematic of thermocouple calibration. The reference junctions are in open air, which is in a temperature-controlled room at 72 F (22.22 C or 295 K).

Once the uncertainty of the thermocouple is found, the Nickel thermometer calibration can be done. Four equally spaced indium dots are placed in a line on a 0.6 mm Nickel bar on a glass slide, similar to Figure 4.1. A lock-in amplifier (an SRS830) is connected to the two inner dots to measure a voltage drop. The waveform generator (a Keysight 33600A) is connected to an outer dot to apply a 0.44 μA AC current (by passing a 30 mV AC voltage

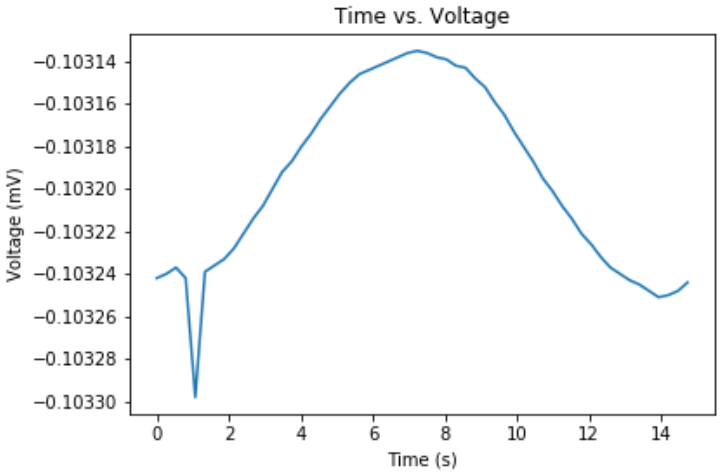

Figure 4.6: 15 second measurement of the thermocouple voltage in open air. The 4E-5 mV standard deviation is taken to be the thermocouple error.

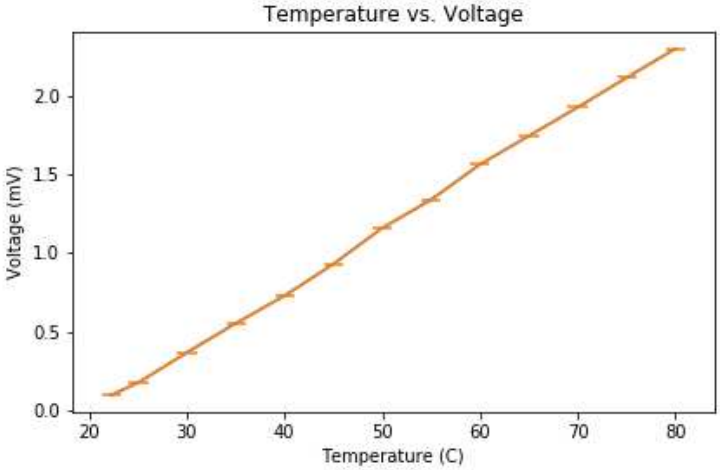

Figure 4.7: Thermocouple calibration line on a hot plate. The error bars in the Voltage are present but too small to see.

in series with a shunt resistor of 68 KΩ). The other outer dot is grounded. A small current is chosen in order to get rid of Joule heating effects. Skin depth effects from the AC signal can be ignored because the films are so thin. The electronics setup is shown in Figure 4.8. A 20 second measurement is taken at room temperature with the SRS while the AC current is being applied through a resistor to see what noise is due to the SRS and waveform generator. Another 20 second measurement is taken with the AC current applied through the Nickel. The SRS outputs the voltage difference between the two dots as well as the error in the voltage difference.

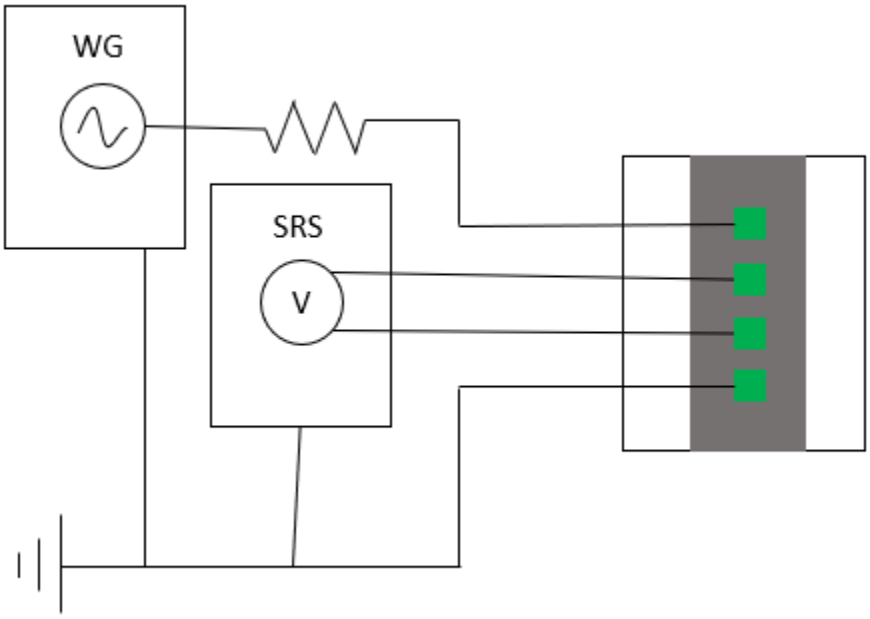

Figure 4.8: Schematic (not to scale) of the Nickel calibration. The green squares are indium dots and the dark grey rectangle is the Nickel, which is on a glass slide.

The Nickel thermometer has to be calibrated separately from the VO_2 or the PZT as both VO_2 and PZT have phase transitions and other properties that could affect the four-point probe calibration measurement of the Nickel. As long as the dimensions of the Nickel bars are the same on each substrate, this is a reasonable assumption.

To fully calibrate the Nickel thermometer, a voltage-temperature curve is made with the Nickel on the glass slide. Measurements are taken below, at, and above room temperature. The setup for the calibration measurements were slightly different between temperatures above and below room temperature due to equipment availability. The electronics setup in Figure 4.8 still applies here. For temperatures above room temperature, the glass substrate with Nickel (cut to the size of the PZT thin film) is placed on a small copper plate. The thermocouple is placed on the copper plate, and this plate is placed on the hot plate, as seen in Figure 4.9. The copper plate has a high thermal conductivity compared to the glass, so the copper will heat up much faster then the glass. After a long enough period of time (about 5-10 minutes), eventually the glass will be the same temperature as the copper plate so that the copper plate temperature the thermocouple measures will approximately the same as the glass and Nickel.

The setup for temperatures below room temperature is a little different. Providing a constant cooling source like a hot plate was unfeasible, so the assumption about the copper plate and glass slide being the same temperature did not hold for this setup. Instead, another glass slide with the same size Nickel bar is used, with glass slide dimensions that are large enough to place the thermocouple on the glass without touching the Nickel bar. The glass is then placed on a larger copper block over ice cubes, as seen in Figure 4.10. The copper block is then taken off the ice cubes to slowly heat up while the thermocouple is able to capture more time-resolved measurements of the glass temperature then in the above-room temperature setup.

The voltage measurements of the Nickel bar calibration are shown below. The slope of Figure 4.11 graph can then be used with the previous calibration measurements to determine the direct correlation between a voltage change measured on the SRS and a temperature change in the Nickel. Unfortunately, the error in this final calibration step with the SRS is most likely to large to resolve the temperature changes expected from the Nickel strain.

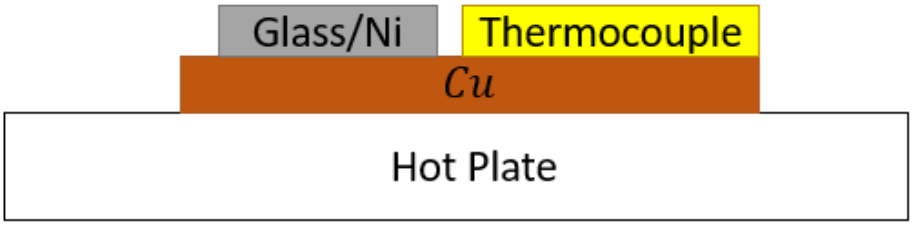

Figure 4.9: Nickel thin film calibration setup for temperatures above room temperature.

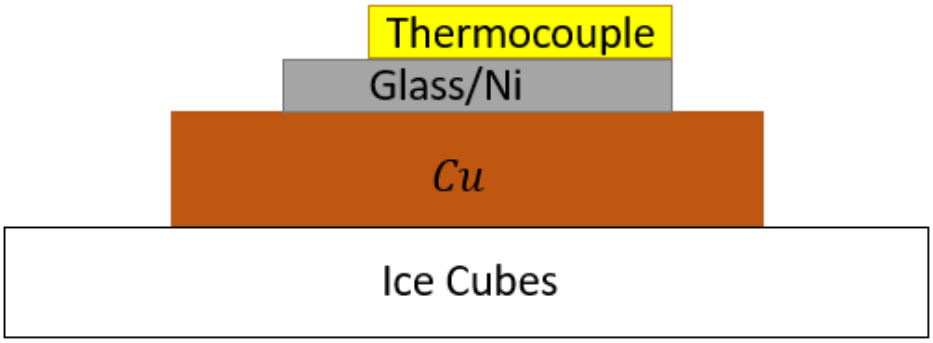

Figure 4.10: Nickel thin film calibration setup for temperatures below room temperature.

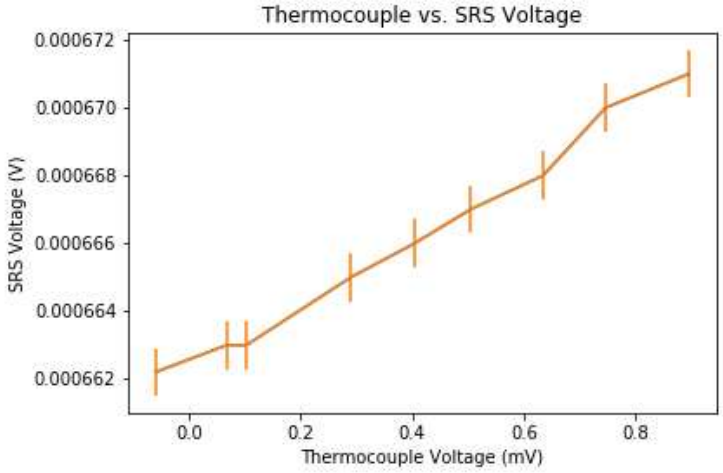

Figure 4.11: Nickel Voltage/Voltage (Thermocouple/SRS) calibration curve. Room temperature is the third data point from left.

Source of Error	ΔT	ΔV
Thermocouple Noise	$1.6 * 10^{-6} C$	N/A
Hot Plate Uncertainty	1 C	N/A
SRS	N/A	$3.43 * 10^{-7}$V
SRS with Indium Dots	N/A	$7 * 10^{-7}$V

Table 4.1: Machine and setup error for temperature and voltage.

4.5.2 Temperature Measurement

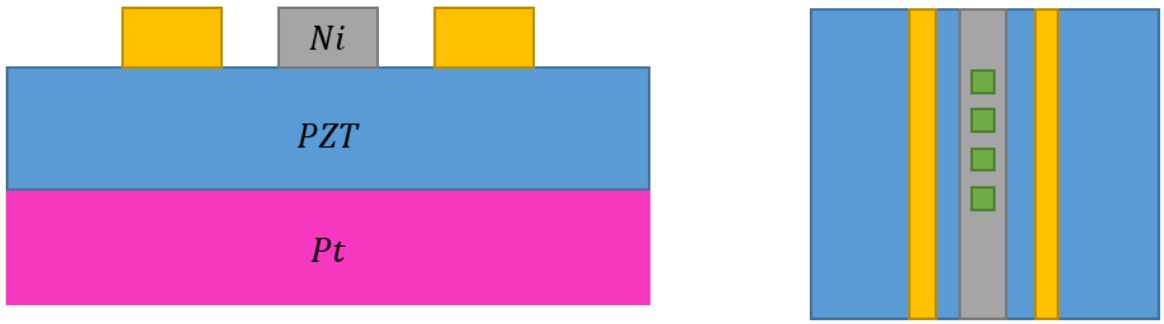

(a) Cross Sectional View

(b) Top View

Figure 4.12: (Left) A cross sectional view and (Right) a top view of the thin film after Nickel deposition and addition of silver paint (yellow) and indium dots (green) to the PZT.

Once the Nickel thermometer is calibrated, the temperature measurement can be performed on the PZT/Ni film. Silver paint lines are added to the surface of the PZT/Ni film in the same fashion as the VO_2 films so that a voltage can be applied across the surface. Four indium dots are attached to the Nickel bar in the same manner as the Nickel calibration, seen in Figure 4.12(a) and Figure 4.12(b). A current source is used to check if all contacts are connected and that the Nickel bar is conducting. The electric field created in the PZT from the silver leads is perpendicular to the direction of current flow and voltage drop of the Nickel bar. The experimental set-up is as follows. A lock-in amplifier (an SRS830) and a waveform generator (a Keysight 33600A) are connected to the PZT/Ni thin film using indium dots and copper wire, just like the Nickel calibration. A voltage source (a Keithley

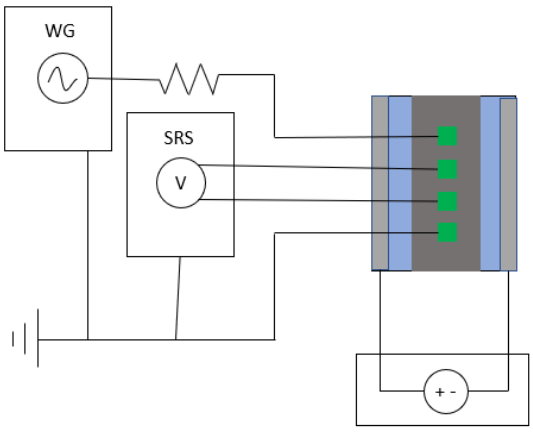

Figure 4.13: schematic

2400) is connected to the PZT portion of the thin film using silver paint and copper wire, like the VO_2 phase transition experiment. A schematic of the setup is depicted in Figure 4.13. A 20 second measurement with the SRS is taken to determine the noise of the system. Then, the waveform generator is turned on, and another 20 second measurement is taken with the SRS for noise. Finally, a 20 second measurement is taken with the SRS, where after 10 seconds, 20 V from the Keithley 2400 is applied. The SRS voltage is average over the first 10 seconds without the 20 V, and over the second 10 seconds with the 20 V. The results are shown in Table 4.2.

	10 sec, 0 V	10 sec, 20 V
Trial 1	$2.9447 * 10^{-5}$V	$2.9455 * 10^{-5}$V
Trial 2	$2.9411 * 10^{-5}$V	$2.9547 * 10^{-5}$V
Trial 3	$1.5079 * 10^{-5}$V	$1.4862 * 10^{-5}$V

Table 4.2: PZT/Ni temperature measurements without and with the 20 V applied across the PZT. Trials 1 and 2 have signal amplitudes of 10 V through the shunt resistor, while Trial 3 has a signal amplitude of 5 V.

4.6 Results and Discussion

A temperature change in the Nickel would be identified from a voltage change in the SRS measurements between the average of the 10 seconds with no voltage and the average of the 10 seconds with 20 V. Unfortunately, the noise from the SRS and the indium dot contacts completely overshadows the comparably small Nickel temperature change. The differences between the 0 and 20 V measurements in Table 4.2 is on the order of magnitude of 10^{-8}V, which is an order of magnitude smaller than the SRS noise of 10^{-7}V. The smallest temperature change that could confidently be determined from the current setup is due to an SRS voltage change of $1 * 10^{-6}$V, just above the SRS noise. This voltage change equates to a change of .11 mV of the thermocouple from the Nickel calibration curve. From the value of .0387 mV/K measured for the thermocouple, this leads to a temperature change of 2.8 K. If there was a temperature change in the Nickel, it was at most 2.8 K, but anything less is within the noise of the setup.

After the measurement, it was discovered that the assumption about calibrating the Nickel on a glass slide (initially based on the premise of using VO_2 as the substrate) and using that calibration curve to interpret data from the Nickel on the PZT does not hold. Using the Nanovoltmeter, the resistance of the Nickel on the glass slide is 20 kΩ. The Nickel on the PZT has a resistance of 300kΩ. For the same dimensions, the resistance of the Nickel is 2 orders of magnitude different, indicating some material property difference, perhaps due to the substrate deposited on. Figure 4.14 shows pictures taken from an AFM of VO_2/Ni bilayers deposited on Al2O3(001), TiO2 (101), and Al2O3(012) substrates. If grain boundaries in the Nickel between those similarly structured substrates varies that much, then the grain boundaries in the Nickel between amorphous glass and crystalline PZT could dramatically alter the grain size and resistance of Nickel.

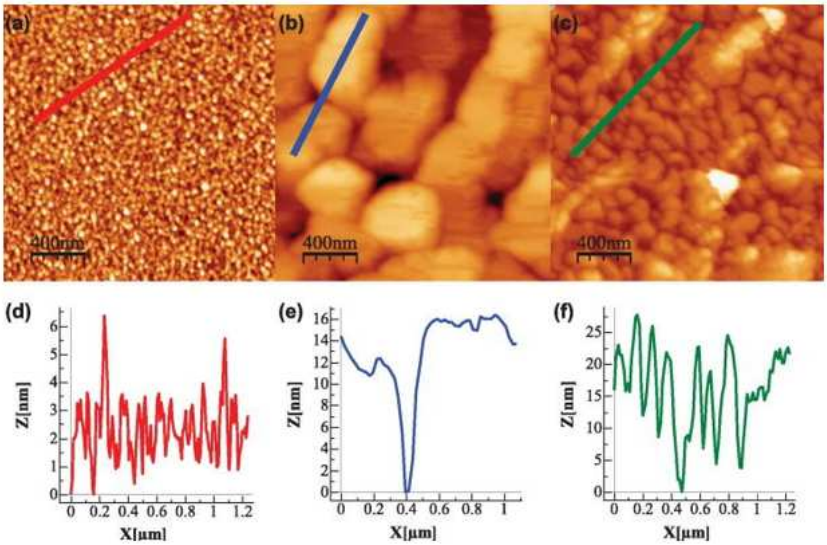

Figure 4.14: Atomic Force Miscroscopy (AFM) images of Nickel grown on multiple substrates, (a) Al2O3(001); (b) TiO2 (101); and (c) Al2O3(012). (d)-(f) are vertical profile lines of the AFM.[5]

4.6.1 Error Analysis

The greatest sources of error are from the SRS connected to the waveform generator, and from the orientation and spacing of the indium dot contacts on the PZT/Ni film. In conducting a four point probe measurement, it is assumed that the size of the contacts are smaller compared to the measured object, that the distance between dots is much smaller than the length of the object, and that the contacts are solely on that object. The ratio between the dot distance and the Nickel bar length is less then 1, but not as small as it could be to reduce noise. Another potential source of error is due to the inconsistent deposition thickness of the Nickel in the sputtering chamber. The sputtering thickness varies linearly with distance from the center of the sample stage. A glass slide used to optimize sputtering parameters with Nickel had a variation of up to 40 nm across the length of the slide. The PZT film is about 1/4 to a 1/5 the length of the slide, so 8-10 nm of difference in thickness while attempting to replicate 15 nm is a significant percentage. It is possible this potential variation in Nickel thickness contributes to the order of magnitude difference in resistance

between the Nickel on the glass slide and the Nickel on the PZT if the PZT Nickel is less thick then the glass Nickel. A thinner deposition could produce a more "pinholey" film, where gaps in the Nickel could oxidize into an insulating oxide, increasing the Nickel resistance. It is also possible that the PZT is pinholey as well, resulting in the same Nickel oxidation.

CHAPTER 5
CONCLUSION AND OUTLOOK

The concept of using alternative methods, like voltage and stress, to drive the MCE for magnetic cooling is plausible but will require future work to find the perfect hybrid system. From this research, several conclusions can be drawn. First, VO_2 as a long-term magnetic cooling substrate is less practical than other candidate materials at this time because of the relatively short life time (3-6 months) of being able to drive the phase transition. This would require addressing future scalability issues, like storage, packaging, and transportation in order to accomodate its short life time. If there is a method to renew the phase transition behavior, potentially with annealing in oxygen or some other method, then VO_2 becomes a more viable candidate material. The voltage driven phase transition of VO_2 is also highly sensitive to material parameters. Even though many characteristics like the temperature driven phase transition and electronic transport properties are similar between sputtered and sol-gel VO_2, there are enough unknown differences in their structures so that the voltage threshold for the phase transition between the sputtered VO_2 film and the sol-gel VO_2 film is at least triple in value. In terms of measuring the temperature change of the VO_2/Ni system using a four point probe, VO_2 requires the Nickel calibration to be on a different substrate because the temperature driven phase transition would skew the calibration, especially above the phase transition temperature when the VO_2 is in its conducting state.

PZT as an MCE material also has its pros and cons, many of which are the opposite of VO_2. PZT is an insulator, so the Nickel calibration can be done while the Nickel is on the PZT. This is actually found to be necessary as the Nickel resistance on PZT vs on the glass is substantially different, in contrast to the VO_2. PZT also has an interesting parameter space to explore in terms of voltage driven stress. There are multiple piezoelectric coefficients of PZT, so if one configuration of electric field direction and four point probe orientation

does not work, there are several other configurations that could prove to be better. Given this experiment, the voltage would need to be increased to improve the magnitude of the stress and temperature change. There is a potential complication in the future of using PZT because it is a ferroelectric. The details of how the ferroelectric effect would play a role in the inverse piezoelectric effect, especially if the voltage needed to produce a sufficient deformation in the PZT is on the order of magnitude of the ferroelectric phase transition, would need to be factored into future device fabrication.

Through preliminary simulations of Nickel under stress, magnetostriction can accomplish the adiabatic demagnetization process in Nickel. If the Nickel has reached its saturation magnetization, whether by a small .1 T magnetic field or some other method, then the previous hybrid systems should conceptually be able to function as magnetic cooling devices, going through the entirety of ADR cycles. Given simulation and experimental results, the current two hybrid devices do not fare well compared to other leading MCE materials, but this is the first material iteration of this new concept. The idea of using magnetic fields to drive the MCE for ADR has been around for decades. Only with further research and iterations can materials systems based on a stress induced MCE be fairly compared with tried and true magnetic field induced MCE materials.

For future work on this project, the most immediate viable experiment is performing the temperature change measurement exactly as described before except with sputtered VO_2 instead of PZT, and assuming a parallel resistance model after the phase transition of VO_2 has occurred to extract the resistance of the Nickel. The other viable experiment mentioned above would be to explore other configurations and orientations of the electric field on the PZT (while instead calibrating the Nickel thermometer on the PZT itself). Reducing noise in the SRS and indium dot connections will be key for these two measurements as that is the greatest source of error in the setup, unless a larger voltage source is used. The simulations could be improved upon as well. The Monte Carlo simulation would benefit from formatting the Nickel into an FCC structure in the <111> orientation. It would also be interesting

to play with more specific magneto-elastic and elastic Hamiltonian terms that describe the structures of the materials used better than universal isotropic terms. If this proves to be too computationally intensive, it may be more fruitful to transfer the entire simulation into LAMMPS as a magnetic spin system package has been added to the LAMMPS repertoire in spring of 2019, performing the calculations the Monte Carlo simulation did and more. The LAMMPS simulation would also benefit from building the VO_2 in the correct orientation, as well as the correct orientation relative to the Nickel. It is also worth exploring if a non-isotropic magnetostriction can be used to isothermally magnetize the Nickel.

In general, the idea of using a substrate with a large deformation with a material that has a high magnetostriction coefficient is conceptually sound, as shown by simulation results. The best material combination for this system would be a substrate with large deformation and a material with high magnetostriction, but also with a high misfit strain between the two materials to maximize the transfer of stress in the deformation into stress/strain into the material. With continued efforts, this material combination can be found.

REFERENCES CITED

[1] J. Berwald. One overlooked way to fight climate change? dispose of old cfcs. *National Geographic- Environment*, 2019.

[2] J. Lyubina. Magnetocaloric materials for energy efficient cooling. *J. Appl. Phys. D*, 50 (5), 2017.

[3] A. Smith et. al. Materials challenges for high performance magnetocaloric refrigeration devices. *Advanced Energy Materials*, 2(11):1288–1318, 2012. doi: 10.1002/aenm.201200167.

[4] V. K. Pecharsky, K. A. Gschneidner, A. O. Pecharsky, and A. M. Tishin. Thermodynamics of the magnetocaloric effect. *Physical Review B - Condensed Matter and Materials Physics*, 2001. ISSN 01631829. doi: 10.1103/PhysRevB.64.144406.

[5] L. Sutton J. Lauzier and J. de la Venta. Coercivity enhancement in vo2/ni bilayers due to interfacial stress. *J. Appl. Phys.*, 122, 2017.

[6] J.P. Joule. Xxxii. on the calorific effects of magneto-electricity, and on the mechanical value of heat. *The London, Edinburgh, and Dublin Philosophical Magazine and Journal of Science*, 23(152):263–276, 1843. doi: 10.1080/14786444308644730.

[7] Smith, A. Who discovered the magnetocaloric effect? - warburg, weiss, and the connection between magnetism and heat. *Eur. Phys. J. H*, 38(4):507–517, 2013. doi: 10.1140/epjh/e2013-40001-9.

[8] W. Thomson. Cyclopedia of the physical sciences 2nd ed. *London and Glasgow*, (838), 1860.

[9] W. Thomson. Ii. on the thermoelastic, thermomagnetic, and pyroelectric properties of matter. *The London, Edinburgh, and Dublin Philosophical Magazine and Journal of Science*, 5(28):4–27, 1878. doi: 10.1080/14786447808639378.

[10] N. Tesla. Pyromagneto-electric generator. US Patent US42805, 1890.

[11] T. Edison. Pyromagnetic generator. US Patent US476983, 1892.

[12] A. Piccard P. Weiss. Sur un nouveau phenomene magnetocalorique. *Comptes Rendus*, (166), 1918.

[13] M.P. Langevin. Magnetisme et theorie des electrons. *Ann. Chim. Phys.*, (5), 1905.

[14] W. F. Giauque and D. P. MacDougall. Attainment of temperatures below 1 absolute by demagnetization of gd2(so4)3.8h2o. *Physical Review - PHYS REV X*, 43:768–768, 01 1933. doi: 10.1103/PhysRev.43.768.

[15] G. V. Brown. Magnetic heat pumping near room temperature. *Journal of Applied Physics*, 47(8):3673–3680, 1976. doi: 10.1063/1.323176.

[16] `http://media.web.britannica.com/eb-media/72/62872-004-040B9E7D.gif`, . Accessed: 2019-3-1.

[17] `https://en.wikipedia.org/wiki/Vapor-compression_refrigeration#/media/File:RefrigerationTS.png`, . Accessed: 2019-3-1.

[18] J. Romero Gmez, R. Ferreiro Garcia, A. De Miguel Catoira, and M. Romero Gmez. Magnetocaloric effect: A review of the thermodynamic cycles in magnetic refrigeration. *Renewable and Sustainable Energy Reviews*, 17:74 – 82, 2013. ISSN 1364-0321.

[19] B.D. Cullity and C.D. Graham. *Introduction to Magnetic Materials*. John Wiley and Sons, 2 edition, 1993.

[20] J. Sirohi and I. Chopra. Fundamental understanding of piezoelectric strain sensors. *J. Intell. Material Syst. Struct.*, 11(4):246–257, 2000.

[21] S. Plimpton. Fast parallel algorithms for short-range molecular dynamics. *J Comp Phys*, 117(1-19), 1995. URL `http://lammps.sandia.gov`.

[22] S.A. Etesami and E. Asadi. *J. Phys. Chem. Solids*, 112(61-72), 2018.

[23] J.L. Zhang B. Grabowski S.B. Maisel, W.S. Ko and J. Neugebauer. *Phys. Rev. Mater.*, 1(3), 2017.

[24] T. Liang K. Choudhary M.J. Noordhoek Y.-T. Cheng S.R. Phillpot A. Kumar, A. Chernatynskiy and S.B. Sinnott. *J. Phys. Condens. Matter*, 27(33), 2015.

[25] C. Kittel. Physical theory of ferromagnetic domains. *Rev. Mod. Phys.*, 21(4), 1949.

[26] R F L Evans *et al.* Atomistic spin model simulations of magnetic nanomaterials. *J. Phys.: Condens. Matter*, 26(103202), 2014.

[27] P. J. von Ranke E. P. Nbrega, N. A. de Oliveira and A. Troper. Monte carlo calculations of the magnetocaloric effect in gd5sixge1x4 compounds. *Physical Review B*, 72(134426), 2005.

[28] R. Zouari *et al.* Monte carlo simulation of the magnetocaloric effect in la23ca13mno3 single crystal. *J. Magn. Magn. Mater.*, 417:401–406, 2016.

[29] R. Zouari *et al.* Monte carlo simulation of magnetocaloric effect in ndmno3 perovskite. *J. Magn. Magn. Mater.*, 401:91–95, 2016.

[30] M. Legendre, B. Sghaier. Curie temperature of nickel. *J Therm Anal Calorim*, 105(1): 141–143, 2011.

[31] H. Pfnr I. Miccoli, F. Edler and C. Tegenkamp. The 100th anniversary of the four-point probe technique: the role of probe geometries in isotropic and anisotropic systems. *J. Phys. Condens. Matter.*, 27(22), 2015.

[32] *Model SR830 DSP Lock-In Amplifier.*

[33] JP Maria G. Brennecka, J. F. Ihlefeld and B. A. Tuttle. Processing technologies for highpermittivity thin films in capacitor applications. *J. Am. Ceram. Soc.*, 93(12):3935–3954, 2010.

[34] L. Sutton J. Lauzier and J. de la Venta. Magnetic irreversibility in vo2/ni bilayers. *J. Phys. Condens. Matter*, 30, 37.

[35] H. Aubin R. Ghosh Y. Liu B. Wu, A. Zimmers and R. Lopez. Electric-field-driven phase transition in vanadium dioxide. *Phys. Rev. B*, 84(241410), 2011.

[36] M. Liu et. al. Terahertz-field-induced insulator-to-metal transition in vanadium dioxide metamaterial. *Nature*, 487:345348.

[37] C.R. Catlow M. Netsianda, P. E. Ngoepe and S. Woodley. The displacive phase transition of vanadium dioxide and the effect of doping with tungsten. *Chem. Mater.*, 20(5), 2008.

APPENDIX A

LAMMPS FORCE FIELDS AND INTERATOMIC POTENTIALS

$$V_{Buckingham}(r) = A_{ij}exp(-\frac{r_{ij}}{\rho_{ij}}) - \frac{C_{ij}}{r_{ij}^6} \tag{A.1}$$

$$V_{morse}(r) = D_{ij}(1 - exp(-\alpha_{ij}(r_{ij} - r_0)))^2 - D_{ij} \tag{A.2}$$

Table A.1: Parameters for the Short-Range Interatomic Potentials[37]

Interaction	A (eV)	$\rho(A)$	C (eV A^6)	Interaction	D (eV)	$\alpha(\mathrm{A}^{-1})$	$\mathrm{r}_0(A)$
$V^+ - O^-$	15585.5	.1941	27.25	$V^+ - V^+$	.5270	11.720	2.620
$O^- - O^-$	23090.8	.2342	29.80				

APPENDIX B

EXAMPLE LAMMPS INPUT FILES

Monoclinic Version:

```
# Input file for bi-layered crystal, Nickle and Vanadium Dioxide, relaxed


# ------------------------ INITIALIZATION ----------------------
clear
units  metal
dimension 3
boundary p p s
atom_style charge



# ------------------------ ATOM DEFINITION -----------------------
# 15nm NI
lattice         fcc 3.52
region upper block 0 9 0 9 4.75 15

#Vanadium, Oxygen, 100nm, Monoclinic
#Vanadium
lattice  custom 1 a1 5.436 0.0 0.0 a2 0.0 4.505 0.0 a3 0.0 0.0 5.434 &
                   basis .0042 .7508 .7548 basis .4958 .7508 .2548
                   basis .5042 .2492 .7452 basis .9958 .2492 .2452
region middle block 0 7 0 7 0 5
```

```
#Oxygen
lattice  custom 1 a1 5.436 0.0 0.0 a2 0.0 4.505 0.0 a3 0.0 0.0 5.434 &
                  basis .2014 .5992 .3991 basis .2017 .1002 .9009
                  basis .2983 .1002 .4009 basis .2986 .5992 .8991
                  basis .7014 .4008 .1009 basis .7017 .8998 .0991
                  basis .7983 .8998 .0991 basis .7986 .4008 .6009
region lower block 0 7 0 7 0 5
region whole union 3 upper middle lower

create_box 3 whole

lattice  fcc 3.52 orient x 1 0 0 orient y 0 1 0 orient z 0 0 1
create_atoms  1 region upper

lattice  custom 1 a1 5.436 0.0 0.0 a2 0.0 4.505 0.0 a3 0.0 0.0 5.434 &
                  basis .0042 .7508 .7548 basis .4958 .7508 .2548
                  basis .5042 .2492 .7452 basis .9958 .2492 .2452
                  orient x 1 0 0 orient y 0 1 0 orient z 0 0 1
create_atoms 2 region middle

lattice  custom 1 a1 5.436 0.0 0.0 a2 0.0 4.505 0.0 a3 0.0 0.0 5.434 &
                  basis .2014 .5992 .3991 basis .2017 .1002 .9009
                  basis .2983 .1002 .4009  basis .2986 .5992 .8991
                  basis .7014 .4008 .1009 basis .7017 .8998 .0991
                  basis .7983 .8998 .0991 basis .7986 .4008 .6009
                  orient x 1 0 0 orient y 0 1 0 orient z 0 0 1
create_atoms 3 region lower
```

```
#read_dump dump.comp 10 x y z box no replace yes # check file names

mass 1 59
mass 2 50.9
mass 3 16

# ------------------------ FORCE FIELDS ----------------------

pair_style hybrid/overlay comb3 polar_off meam morse 3.0 buck 3.0
pair_coeff * * comb3 ffield.comb3.NiAlO Ni NULL O
pair_coeff * * meam library.meam Ni V VNiTi.meam Ni V NULL
pair_coeff 2 2 morse .5270 11.720 2.620
pair_coeff 2 3 buck 15585.5 .1941 27.25
pair_coeff 3 3 buck 23090.5 .2030 30.00
pair_coeff * * meam library.Ni.meam Ni Ni.meam Ni NULL NULL

#---------------------------Settings-----------------------------
compute csym all centro/atom fcc
compute eng all pe/atom
compute eatoms all reduce sum c_eng
compute strs all stress/atom NULL

#----------------------Run Minimization-------------------------
#set temp
reset_timestep 0
fix 1 all nvt temp 300.0 300.0 $(100.0*dt)
```

```
thermo 10
thermo_style custom step pe lx ly lz press pxx pyy pzz c_eatoms
dump 1 all custom 10 dump.comp.*
id type mass xs ys zs c_csym c_eng c_strs[1] c_strs[2] c_strs[3]
min_style cg
minimize 1e-15 1e-15 5000 5000

print "All done!"

########################################

# SIMULATION DONE
print "All done"
```

Tetragonal Version:

```
# Input file for bi-layered crystal, Nickle and Vanadium Dioxide, relaxed

# ------------------------ INITIALIZATION ----------------------
clear
units  metal
dimension 3
boundary p p s
atom_style charge



# ----------------------- ATOM DEFINITION -----------------------
# 15nm NI
lattice         fcc 3.52
region upper block 0 9 0 9 9.5 20

#Vanadium, Oxygen, 100nm, Tetragonal
#Vanadium
lattice  custom 1 a1 4.55 0.0 0.0 a2 0.0 4.55 0.0 a3 0.0 0.0 2.86 &
                  basis 0.0 0.0 0.0 basis 0.5 0.5 0.5
region middle block 0 7 0 7 0 10

#Oxygen
lattice  custom 1 a1 4.55 0.0 0.0 a2 0.0 4.55 0.0 a3 0.0 0.0 2.86 &
                  basis 0.799435 0.200565 0.500000
                  basis 0.200565 0.799435 0.500000
                  basis 0.700565 0.700565 0.000000
```

```
                    basis 0.299435 0.299435 0.000000
region lower block 0 7 0 7 0 10
region whole union 3 upper middle lower

create_box 3 whole

lattice  fcc 3.52 orient x 1 0 0 orient y 0 1 0 orient z 0 0 1
create_atoms 1 region upper

lattice  custom 1 a1 4.55 0.0 0.0 a2 0.0 4.55 0.0 a3 0.0 0.0 2.86 &
                    basis 0.0 0.0 0.0 basis 0.5 0.5 0.5
                    orient x 1 0 0 orient y 0 1 0 orient z 0 0 1
create_atoms 2 region middle

lattice  custom 1 a1 4.55 0.0 0.0 a2 0.0 4.55 0.0 a3 0.0 0.0 2.86 &
                    basis 0.799435 0.200565 0.500000
                    basis 0.200565 0.799435 0.500000
                    basis 0.700565 0.700565 0.000000
                    basis 0.299435 0.299435 0.000000
                    orient x 1 0 0 orient y 0 1 0 orient z 0 0 1
create_atoms 3 region lower

mass 1 59
mass 2 50.9
mass 3 16

# ----------------------- FORCE FIELDS ----------------------
```

```
#Ni-O
#pair_style comb3 polar_off
#pair_coeff * * ffield.comb3.NiAlO Ni O

#V-Ni
#pair_style meam
#pair_coeff * * library.meam Ni V VNiTi.meam Ni V

#V-O
#pair_style buck 3.0
#pair_coeff * * 15585.5 .1941 27.25

pair_style hybrid/overlay comb3 polar_off meam morse 3.0 buck 3.0
pair_coeff * * comb3 ffield.comb3.NiAlO Ni NULL O
pair_coeff * * meam library.meam Ni V VNiTi.meam Ni V NULL
pair_coeff 2 2 morse .5270 11.720 2.620
pair_coeff 2 3 buck 15585.5 .1941 27.25
pair_coeff 3 3 buck 23090.5 .2030 30.00
pair_coeff * * meam library.Ni.meam Ni Ni.meam Ni NULL NULL

#---------------------------Settings-----------------------------
compute csym all centro/atom fcc
compute eng all pe/atom
compute eatoms all reduce sum c_eng
compute strs all stress/atom NULL

#----------------------Run Minimization-------------------------
```

```
#set temp
reset_timestep 0
fix 1 all nvt temp 300.0 300.0 $(100.0*dt)
thermo 10
thermo_style custom step pe lx ly lz press pxx pyy pzz c_eatoms
dump 1 all custom 10 dump.comp.*
id type mass xs ys zs c_csym c_eng c_strs[1] c_strs[2] c_strs[3]
min_style cg
minimize 1e-15 1e-15 5000 5000

print "All done!"

########################################

# SIMULATION DONE
print "All done"
```

APPENDIX C

X, Y, AND Z COMPONENTS OF MAGNETIZATION

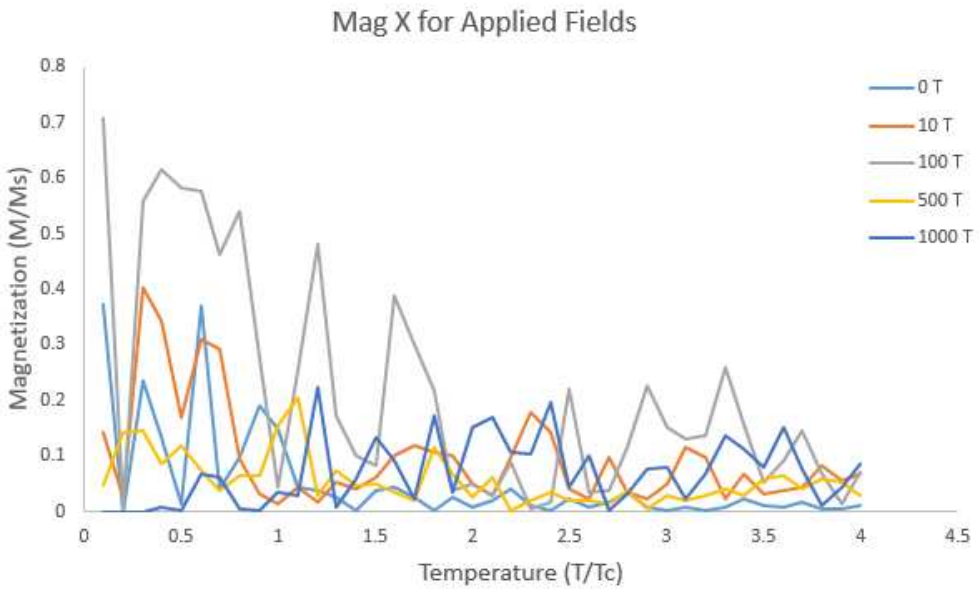

Figure C.1: Magnetization in the x direction vs. temperature with various applied magnetic fields. The system is 3x3x3 with 200 MCS.

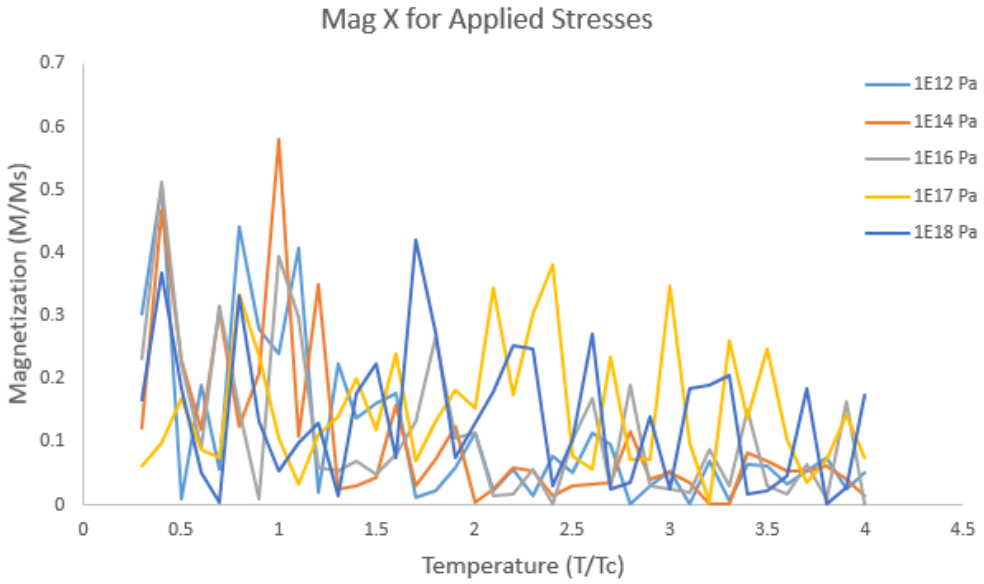

Figure C.2: Magnetization in the x direction vs. temperature with various applied stresses. The system is 3x3x3 with 200 MCS.

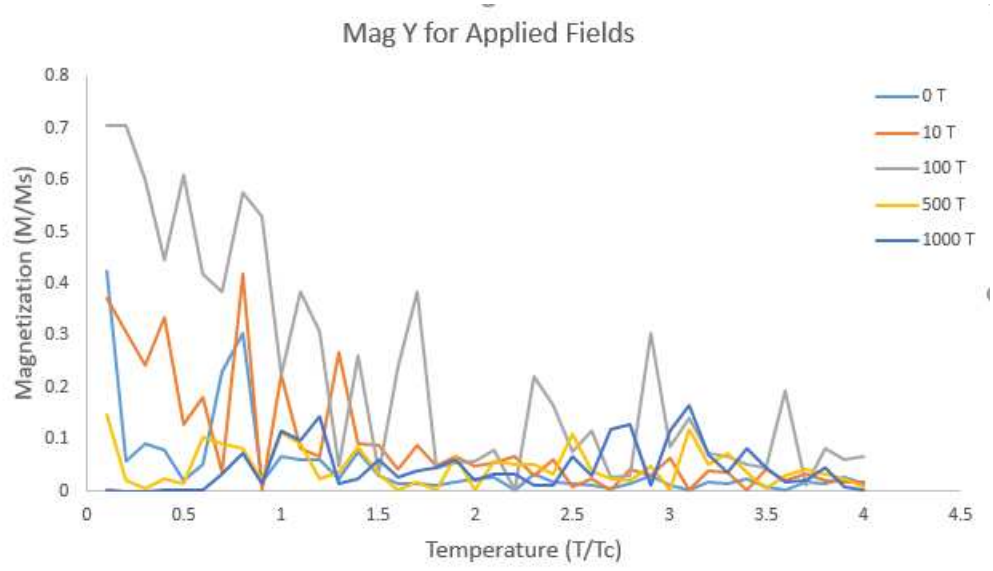

Figure C.3: Magnetization in the y direction vs. temperature with various applied magnetic fields. The system is 3x3x3 with 200 MCS.

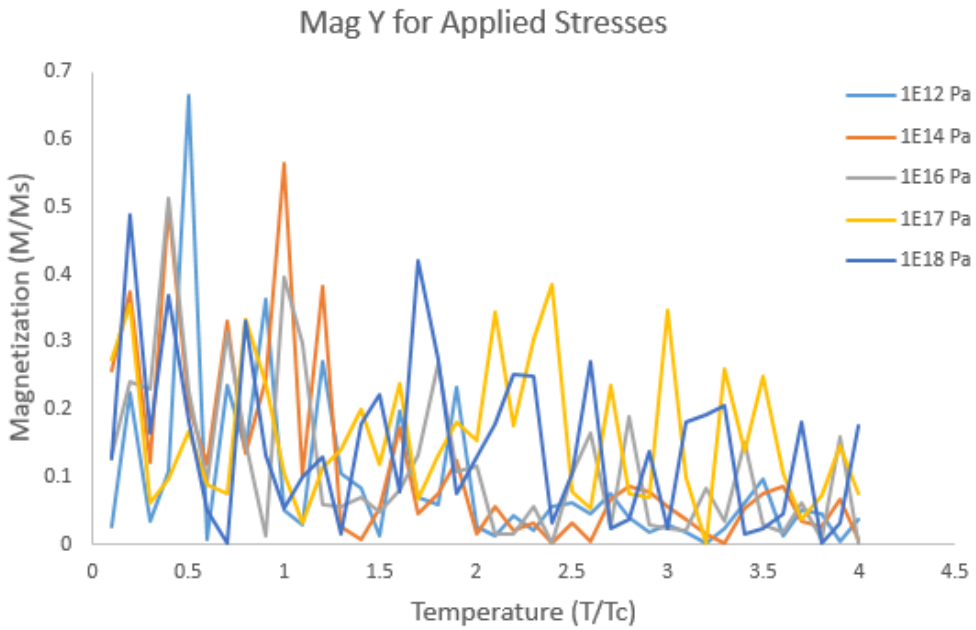

Figure C.4: Magnetization in the y direction vs. temperature with various applied stresses. The system is 3x3x3 with 200 MCS.

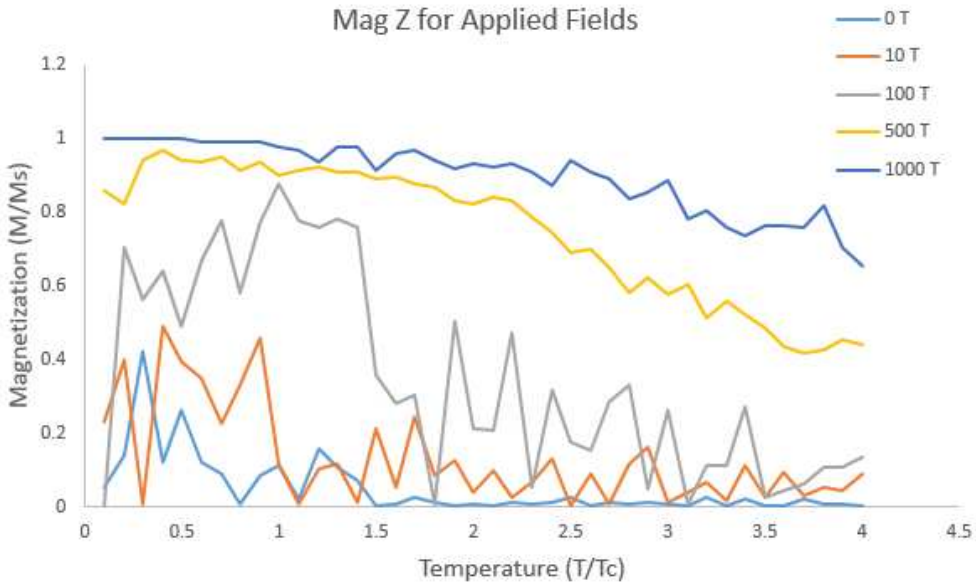

Figure C.5: Magnetization in the z direction vs. temperature with various applied magnetic fields. The system is 3x3x3 with 200 MCS.

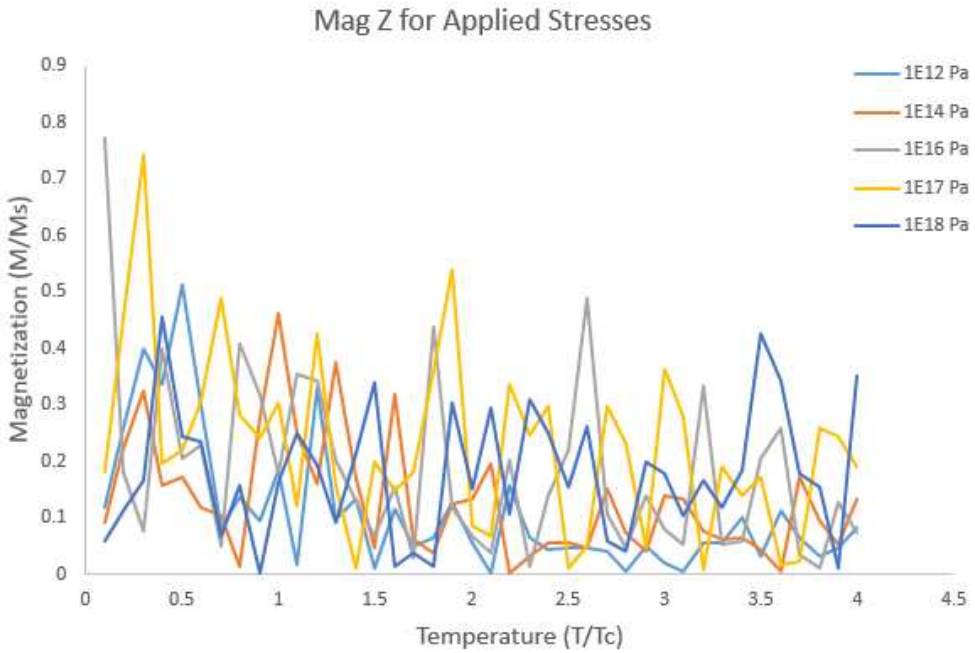

Figure C.6: Magnetization in the z direction vs. temperature with various applied stresses. The system is 3x3x3 with 200 MCS.

APPENDIX D

ΔS AND ΔT PLOTS

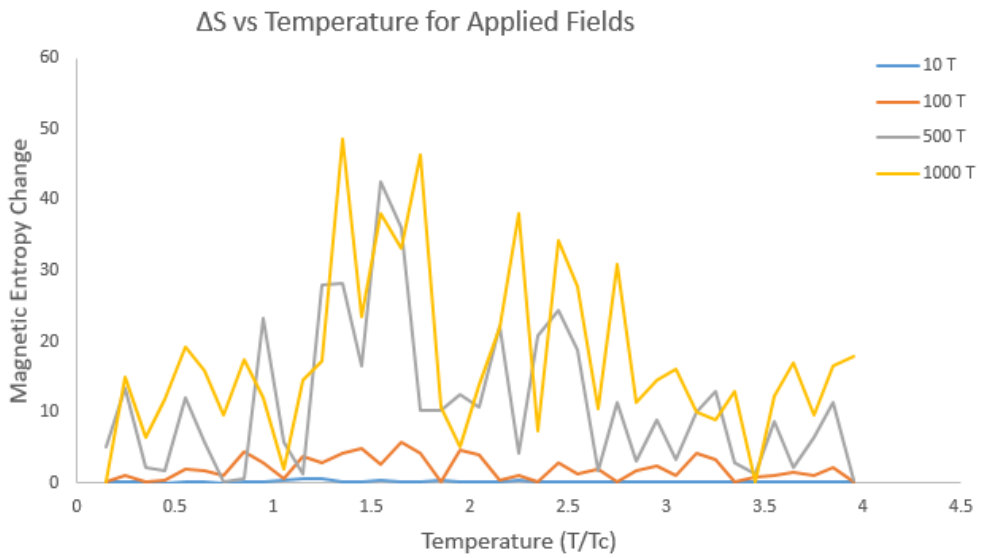

Figure D.1: Change in magnetic entropy vs. temperature for various applied magnetic fields. The system is 3x3x3 with 200 MCS.

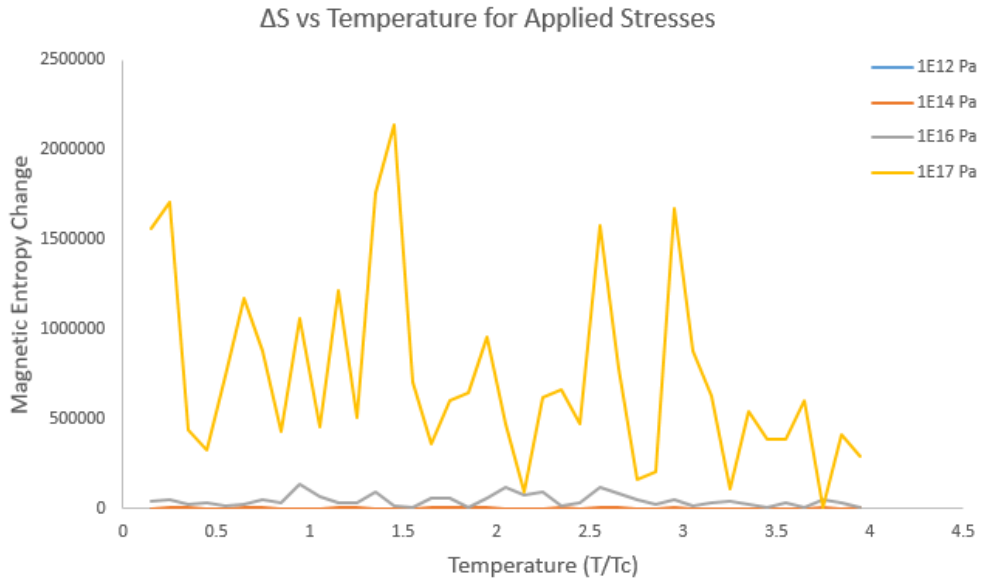

Figure D.2: Change in magnetic entropy vs. temperature for various applied stresses. The system is 3x3x3 with 200 MCS.

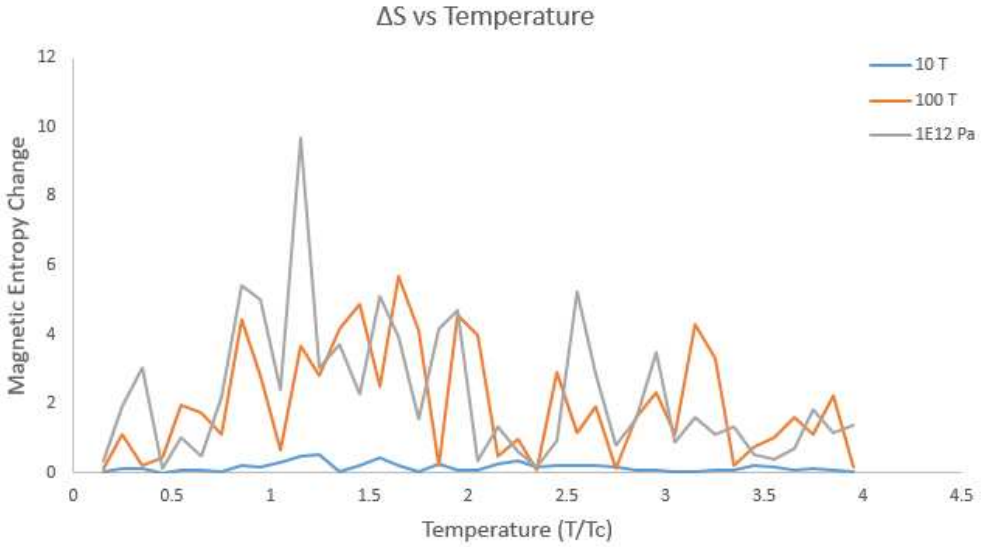

Figure D.3: Change in magnetic entropy vs. temperature for an applied field and an applied stress. The system is 3x3x3 with 200 MCS.

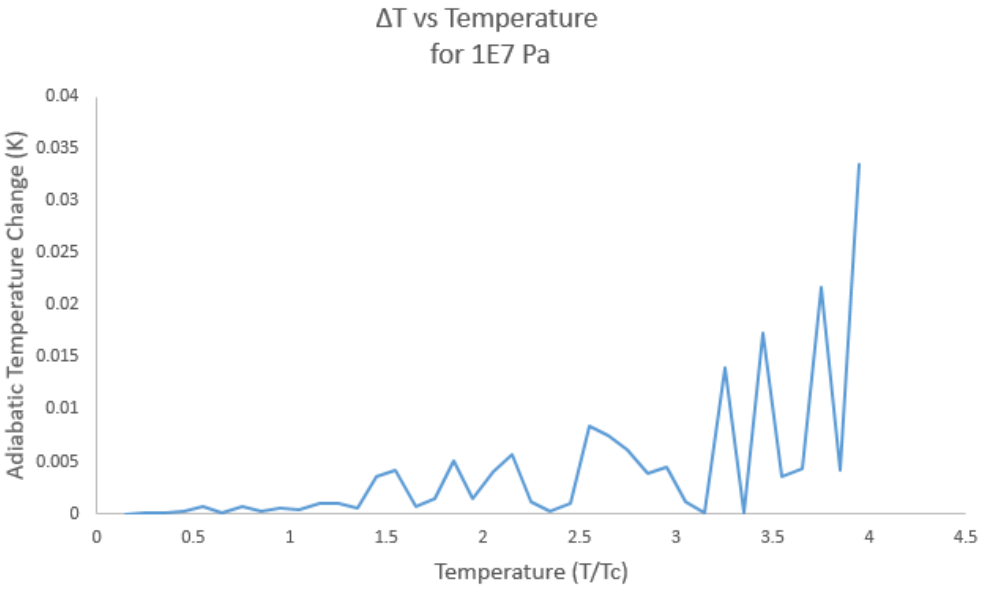

Figure D.4: Adiabatic temperature change vs. temperature for an applied stress. The system is 3x3x3 with 200 MCS.

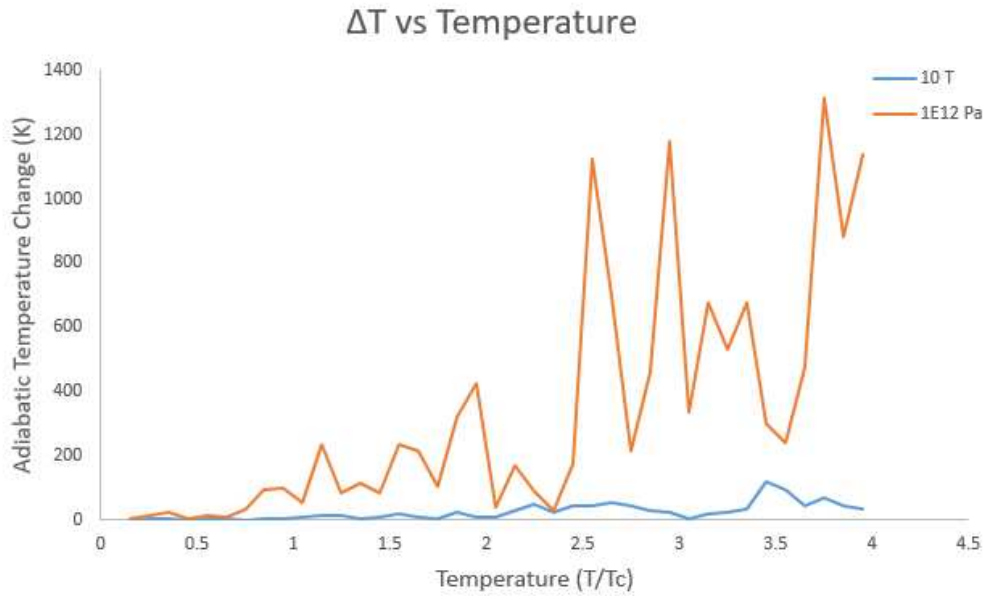

Figure D.5: Adiabatic temperature change vs. temperature for an applied field and an applied stress. The system is 3x3x3 with 200 MCS.